Table 1 Characteristics of patients and laboratory data

Patient no.	Sex	Age	Therapy condition	Past operation	Symptom	IPI	WBC	CRP	LDH	sIL2	TKA	EBNA antibody
1	F	79	Initial	NP	Fever	1	7570	14.75	141	775	5.2	160
2	M	77	Recurrence	NP	Chest pain	1	6010	2.81	212	588	18.2	320
3	M	76	Recurrence	AP	Chest pain	1	7240	6.69	228	407	8.5	10
4	M	73	Initial	AP	Chest pain	2	7910	2.83	192	690	5.9	10
5	M	71	Initial	AP	Chest pain, fever	2	9160	10.34	300	958	11.4	NA
6	F	87	Initial	AP	Chest pain, fever	2	10430	3.15	271	694	7.1	320
7	M	80	Initial	AP	Chest pain	3	12160	3.75	338	1138	16.1	320

AP artificial pneumothorax, *NP* not performed, *IPI* international prognostic index, *WBC* white blood cell count, *CRP* C-reactive protein, *LDH* lactate dehydrogenase, *sIL2R* soluble interleukin 2 receptor, *TKA* thymidine kinase activity, *EBNA* EBV nuclear antigen, *NA* not available

Table 2 Condition and imaging characteristics on PET/CT

No.	Indication for PET/CT or PET	Therapy and condition	SUVmax	Decrease %SUVmax	Non-enhanced CT contribution to PET/CT
1	Staging	Initial staging	34.2		Chest wall swelling
	Response	Response to irradiation (56 Gy)	1.1	−97	Shrinking of swelling chest wall
	Follow-up	Follow-up	1.4		No contribution
2	Restaging	Local recurrence	14.2		Chest wall swelling
	Response	Response to irradiation (40 Gy)	2.2	−84	Chest wall swelling
	Restaging	Local recurrence	16.6		Destruction of ribs
	Response	Response to R-CHOP	19.9	+20	Destruction of ribs and chest wall invasion
3	Restaging	Local recurrence	21.2		Mass with chest wall invasion and destruction of calcified wall in CP
	Response	Response to irradiation (54 Gy)	4.6	−78	To detect shrinking tumor
	Restaging	Local recurrence	17.2		To detect tumor regrowth
	Response	Response to irradiation (50 Gy)	5.1	−70	To detect shrinking tumor
	Restaging	Local recurrence	8.3		To detect tumor regrowth
4	Staging	Initial staging	18		Mass lesion surrounds the rib
	Response	Response to irradiation (52 Gy)	1.8	−90	Mass lesion surrounds the rib
	Follow-up	Follow-up	1.64		No contribution
5	Diagnosis		27.1		Mass with mediastinum invasion
6	Staging	Initial staging	31.8		Expanding mass and destruction of calcified wall in CP
	Response	Response to irradiation (60 Gy)	3.3	−90	To detect shrinking tumor
	Follow-up	Follow-up	1.6		No contribution
7	Staging	Initial staging	25.7		Mass with chest wall invasion and destruction of calcified wall in CP
	Response	Response to R-CHOP	31.6	+23	To detect tumor growth
	Response	Response to irradiation (60 Gy)	2.1	−93	To detect shrinking tumor
	Restaging	Adrenal gland metastasis	19.1		To detect the right adrenal gland swelling
	Response	Multiple metastases	22.8		No contribution

R-CHOP rituximab with cyclophosphamide, doxorubicin, vincristine and prednisone, *CP* chronic pyothorax

high FDG uptakes at the sites of active inflammation or post-therapy inflammatory changes in pyothorax at the time of the PET/CT scans.

FDG PET/CT was performed in a total of 24 cases for different indications in different patients as shown in Table 2 and below.

Diagnosis and initial staging

Five FDG PET/CT cases were diagnosed with PAL and staged with the help of FDG PET/CT. All of the PET/CT scans detected well-defined masses with intensive FDG uptakes and were positive on visual interpretation. Non-enhanced CT findings during PET/CT examination showed several characteristics reported in previous studies. In this study, non-enhanced CT images on initial PET/CT showed invasion or deviation of structures adjacent to the tumor (chest wall in 3 patients, diaphragm in 1 and pericardium in 1) and destruction of the calcifying shell in three patients (Fig. 1).

One PET/CT examination detected bilateral adrenal metastases in a patient (No. 7) and chemotherapy [rituximab with cyclophosphamide, doxorubicin, vincristine and prednisone (R-CHOP)] was performed as an initial therapy. Three patients (No. 1, 4 and 6) were treated with radiotherapy because PET/CT findings and other modalities showed solitary lesions. One patient (No. 5) could not receive treatment due to a severe physical condition and PAL was diagnosed with autopsy 2 weeks after the initial PET/CT.

Restaging and follow-up

Three patients (No. 2, 3 and 7) in six PET/CT cases had repeat PET/CT performed to evaluate restaging because recurrence was suspected on the basis of physical findings or other imaging modalities in the follow-up period after completion of treatment. At the PET/CT examinations, two patients (No. 2 and 3) had a history of radiotherapy 5 and 6 years earlier, respectively. They had achieved CR until the suspicion of recurrence. They received initial PET/CT examinations to evaluate the restaging (Fig. 1). In one patient (No. 7), PET/CT for restaging was performed after radiotherapy following chemotherapy. PET/CT detected a recurrence in the left adrenal gland.

Three PET/CT scans in three patients (No. 1, 4 and 6) were performed to follow up lesions, and these scans showed no sign of recurrence.

Treatment response evaluation

A total of 10 PET/CT scans in 6 patients (No. 1, 2, 3, 4, 6, and 7) were performed to evaluate the efficacy of treatment. All of them had received radiotherapy or chemotherapy for the PAL lesions before the PET/CT examinations. Five PET/CT scans in 5 patients (No. 1, 2, 4, 6, and 7) showed the same or lower FDG uptake compared with the blood pool or mediastinal uptake, and we considered that the PAL had achieved CR based on the PET/CT findings. Two PET/CT scans in one patient (No. 3) showed relatively higher FDG uptake than blood pool or mediastinal uptake, and these scans were considered to indicate partial response (PR). Two PET/CT scans in 2 patients (No. 2 and 7) showed clearly higher FDG uptakes of the original lesions than previous PET/CT for staging or restaging, and one PET/CT scan (No. 7) detected a new lesion at the scalp. Finally, these three

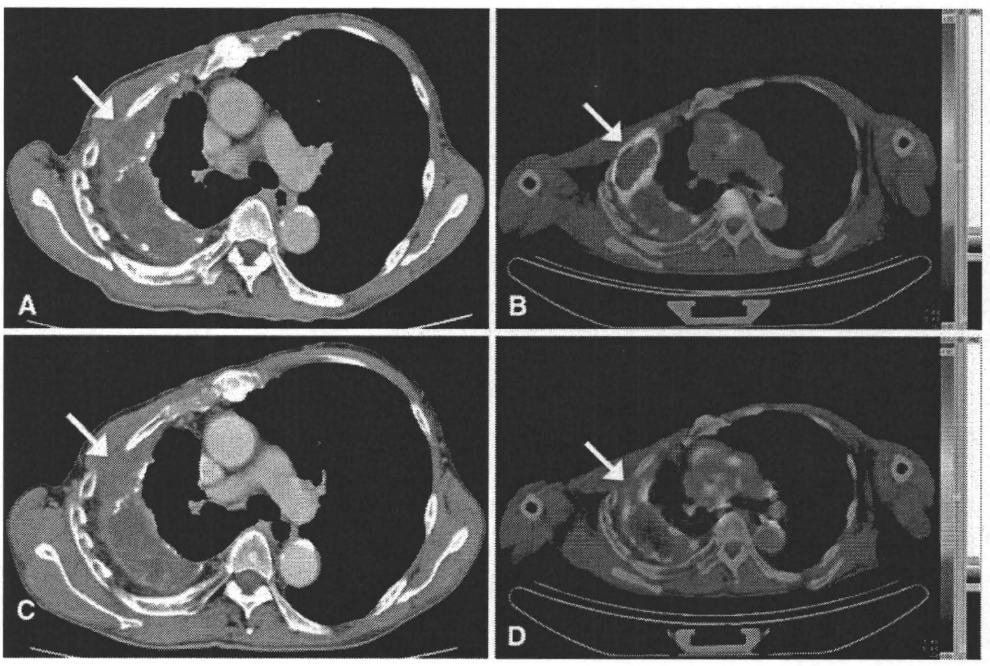

Fig. 1 A 73-year-old man (case 4) with PAL. **a** An axial enhanced CT image shows the enhanced tumor adjacent to the wall of the CP (*white arrow*). **b** Axial FDG PET/CT image shows increased FDG uptake (SUVmax 18.0) at the chest wall with soft tissue density (*white arrow*). **c** After radiotherapy, an axial enhanced CT image shows indistinct findings of a tumor adjacent to the wall of the CP (*white arrow*). **d** After radiotherapy, an axial FDG PET/CT image shows decreased FDG uptake (SUVmax 1.8) at the chest wall with soft tissue density (*white arrow*)

scans were considered to indicate progressive disease (PD).

Change of FDG uptake and CT contribution during PET/CT examination

The decrease percentage of the SUVmax in pre- and post-treatment was calculated from 10 pairs of PET/CT. Imaging results are summarized in Table 2. The SUVmax of the tumor before the initial treatment ranged from 14.2 to 32.5 (mean ± SD, 24.6 ± 7.2). In these patients, the SUVmax of the tumor did not correlate with any of the laboratory data. In the therapeutic efficacy, over 80% decreasing and around 20% increasing uptakes of SUVmax corresponded to CR and PD in our visual interpretation, respectively.

Tumor shape before and after treatment on enhanced CT imaging

The changes of tumor size, shape or enhancement pattern on enhanced CT imaging in the situation of effective treatment are shown in Table 3. The mean interval between the contrast-enhanced CT examinations and the PET/CT examinations was within 6 weeks. On all post-treatment sites except one, residual masses were still identified by enhanced CT imaging, although these lesions shrank in size and showed decreased enhancement. Only one lesion, which was evaluated as CR, became unmeasurable after treatment.

Discussion

PAL is a rare form of malignant lymphoma arising in the pleural wall after a long-standing history of CP [1–3]. Several studies have reported PAL to be associated with EBV infection [4–7]. PAL patients are generally elderly men. PAL occurs throughout the world, but has a high prevalence among Asians who have undergone artificial pneumothorax for pulmonary tuberculosis [13]. As to pathological characteristics, more than 90% of cases showed diffuse B cell lymphoma. Optimal management of PAL is undefined, though several studies have reported various methods of chemotherapy and/or radiotherapy [2, 3, 14]. PAL has a poor prognosis with <40% survival [1, 2].

PAL is occasionally misdiagnosed as lung cancer or a form of tuberculous abscess because of the similarity of the clinical symptoms and radiological findings of these conditions. Contrast-enhanced CT findings have been reported for the diagnosis of PAL, although specific CT diagnostic findings may not be confirmed [8–10]. A few reports have shown the usefulness of 67 gallium citrate (67 Ga) scintigraphy for the diagnosis and assessment of therapeutic effects in PAL cases [8–10, 14, 15]. Recently, there have been a few case reports of ^{18}F-FDG PET findings in patients with PAL [11, 16]. FDG PET imaging, including SUVmax, is useful for diagnosis and assessment of the efficacy of treatment in malignant lymphoma, and has been found to be superior to 67 Ga scintigraphy [17, 18]. Our study also showed FDG PET/CT to be a useful modality for diagnosing PAL and assessing the efficacy of treatment.

Table 3 Enhanced CT findings of PAL and chronic pyothorax

Patient no.	Tumor characteristics on enhanced CT examinations						Chronic pyothorax	
	Location	Growth pattern	Sharp and enhancement patterns in effective treatment		Size (mm)		Location	Shape and carcificated pattern
			Pre-treatment	Post-treatment	Pre-treatment	Post-treatment		
1	Pleura at costophrenic angle	External	Nodular/ inhomogeneous	Disappeared/ disappeared	33 × 15	Non-measurable	Bilateral	Crescent/ circular
2	Lateral costal pleura	External	Nodular/ circumscribed	Nodular/ inhomogeneous	67 × 20	59 × 20	Right	Crescent/ partial
3	Lateral costal pleura	External	Nodular/ circumscribed	Nodular/ circumscribed	56 × 16	47 × 16	Left	Lenticular/ circular
4	Lateral costal pleura	External	Nodular/ inhomogeneous	Nodular/ disappeared	62 × 30	60 × 27	Right	Crescent/ partial
5	Mediastinal pleura	External	Multilocular/ inhomogeneous	–	91 × 47	–	Right	Lenticular/ partial
6	Lateral costal pleura	Symmetric	Nodular/ circumscribed	Nodular/ circumscribed	82 × 47	35 × 23	Left	Crescent/ circular
7	Pleura at costophrenic angle	External	Multilocular/ inhomogeneous	Nodular/ circumscribed	74 × 59	67 × 33	Right	Lenticular/ partial

As an additional advantage, non-enhanced CT imaging during FDG PET/CT facilitates the diagnosis of PAL as a complementary modality for detecting masses or an irregularly shaped CP. Meanwhile, enhanced CT is a useful modality for diagnosing PAL based on the shape or enhancement of lesions. In this study, however, enhanced CT frequently showed residual masses in the post-treatment state, and these residual masses interfered with the accurate decision-making of the therapeutic efficacy. Our study suggests that FDG PET/CT may be an ideal modality for reducing the false-positive interpretation of residual masses occurring after treatment for PAL because of the simultaneous information obtained during PET and CT imaging.

The first limitation of this study is the small size of the study population. However, PAL is a rare form of malignant lymphoma even in Japan. Thus, opportunities to study FDG PET/CT images obtained from patients with PAL are rare. Moreover, this limitation is unlikely to have affected our conclusion, since the usefulness of PET for other types of malignant lymphoma has been clearly demonstrated in previous studies. A second limitation is the short interval between the time after the treatment period and PET/CT examinations. Certainly, post-therapy inflammatory changes may also be observed in clinical lymphoma PET studies for at least 2–3 months after radiation therapy or chemotherapy. To minimize the frequency of these changes, which potentially confound the interpretation of PET scans, PET should preferably not be performed before 8–12 weeks after completion of radiotherapy [12]. However, we were able to accurately interpret the CR states using PET/CT during the earlier periods after treatment. Tangential irradiation for reducing the area of the irradiation field was performed on the patients because PAL lesions were located in peripheral areas of the CP. We considered that this technique might shrink the area of post-therapy inflammatory changes. Moreover the treatment strategy for these patients had to be decided promptly because of the poor prognosis of PAL.

In conclusion, this study showed FDG PET/CT imaging to be useful for various situations in PAL (diagnosis, assessing the efficacy of treatment, restaging and follow-up) even in cases with residual masses. Additionally, SUVmax provides complementary information for the management of PAL.

References

1. Iuchi K, Ichimiya A, Akashi A, Mizuta T, Lee YE, Tada H, et al. Non-Hodgkin's lymphoma of the pleural cavity developing from long-standing pyothorax. Cancer. 1987;60:1771–5.
2. Narimatsu H, Ota Y, Kama M, Takeuchi K, Suzuki R, Matsuo K, et al. Clinicopathological features of pyothorax-associated lymphoma; a retrospective survey involving 98 patients. Ann Oncol. 2007;18:122–8.
3. Nakatsuka S, Yao M, Hoshida Y, Yamamoto S, Iuchi K, Azusa K. Pyothorax-associated lymphoma: a review of 106 cases. J Clin Oncol. 2002;20:4255–60.
4. Fukayama M, Ibuka T, Hayashi Y, Ooba T, Koike M, Mizutani S. Epstein–Barr virus in pyothorax-associated pleural lymphoma. Am J Pathol. 1993;143:1044–9.
5. Sasajima Y, Yamabe H, Kobashi Y, Hirai K, Mori S. High expression of the Epstein–Barr virus latent protein EB nuclear antigen-2 on pyothorax-associated lymphomas. Am J Pathol. 1993;143:1280–5.
6. Takakuwa T, Luo WJ, Ham MF, Mizuki M, Iuchi K, Aozasa K. Establishment and characterization of unique cell lines derived from pyothorax-associated lymphoma which develops in long-standing pyothorax and is strongly associated with Epstein–Barr virus infection. Cancer Sci. 2003;94:858–63.
7. Takakuwa T, Tresnasari K, Rahadiani N, Miwa H, Daibata M, Aozasa K. Cell origin of pyothorax-associated lymphoma: a lymphoma strongly associated with Epstein–Barr virus infection. Leukemia. 2008;22:620–7.
8. Lee HY, Goo JM, Lee HJ, Lee CH, Chun EJ, Im JG. The value of computed tomography for predicting empyema-associated malignancy. J Comput Assist Tomogr. 2006;30:453–9.
9. Ueda T, Andreas C, Itami J, Miyakawa K, Fujimoto H, Ito H, et al. Pyothorax-associated lymphoma: imaging findings. AJR Am J Roentgenol. 2010;194:76–84.
10. Minami M, Kawauchi N, Yoshikawa K, Itai Y, Kokubo T, Iguchi M, et al. Malignancy associated with chronic empyema: radiologic assessment. Radiology. 1991;178:417–23.
11. Asakura H, Togami T, Mitani M, Takashima H, Yokoe K, Yamamoto Y, et al. Usefulness of FDG-PET imaging for the radiotherapy treatment planning of pyothorax-associated lymphoma. Ann Nucl Med. 2005;19:725–8.
12. Juweid ME, Stroobants S, Hoekstra OS, Mottaghy FM, Dietlein M, Guermazi A, Imaging Subcommittee of International Harmonization Project in Lymphoma, et al. Use of positron emission tomography for response assessment of lymphoma: consensus of the Imaging Subcommittee of International Harmonization Project in Lymphoma. J Clin Oncol. 2007;25:571–8.
13. Androulaki A, Drakos E, Hatzianastassiou D, Vgenopoulou S, Gazouli M, Korkolopoulou P, et al. Pyothorax-associated lymphoma (PAL): a western case with marked angiocentricity and review of the literature. Histopathology. 2004;44:69–76.
14. Aruga T, Itami J, Nakajima K, Shibata K, Nojo T, Aruga M, et al. Treatment for pyothorax-associated lymphoma. Radiother Oncol. 2000;56:59–63.
15. Suga K, Ishikawa Y, Motoyama K, Fujimura N, Suda H, Matsunaga N. Ga-67-avid non-Hodgkin's lymphoma arising from chronic nontuberculous pyothorax. Clin Nucl Med. 2001; 26:247–8.
16. Oh JK, Ahn MI, Kim CH, Cho KD, Cho DG, Kang CU, et al. The value of F-18 FDG-PET/CT in diagnosis of chronic empyema-associated malignancy. Clin Radiol. 2008;63:1177–80.
17. Kostakoglu L, Goldsmith SJ. Fluorine-18 fluorodeoxyglucose positron emission tomography in the staging and follow-up of lymphoma: is it time to shift gears? Eur J Nucl Med. 2000; 27:1564–78.
18. Kostakoglu L, Leonard JP, Kuji I, Coleman M, Vallabhajosula S, Goldsmith SJ. Comparison of fluorine-18 fluorodeoxyglucose positron emission tomography and Ga-67 scintigraphy in evaluation of lymphoma. Cancer. 2002;94:879–88.

Pyothorax-Associated Lymphoma: Imaging Findings

Takuya Ueda[1]
Christe Andreas[1]
Jun Itami[2]
Kunihisa Miyakawa[3]
Hajime Fujimoto[4]
Hisao Ito[5]
Justus E. Roos[1]

OBJECTIVE. The purpose of this study was to evaluate the radiologic features of pyothorax-associated lymphoma on CT scans and chest radiographs.

MATERIALS AND METHODS. Radiographs and CT scans of 21 patients with biopsy-proven pyothorax-associated lymphoma (17 men, four women; median age, 71 years; range 52–77 years) were retrospectively identified. Two readers in consensus analyzed the morphologic imaging features of pyothorax-associated lymphoma and determined their relation to the preexisting chronic empyema cavity. In 13 cases, gallium scans were available and were reviewed.

RESULTS. Sixteen patients had a history of artificial pneumothorax therapy for tuberculosis. Pyothorax-associated lymphoma was visualized mainly (71.4% of cases) as extrapulmonary pleural masses on chest radiographs. The CT features included a lenticular (60%) or crescentic (20%) soft-tissue mass located eccentrically at the margin of a coexistent empyema cavity, which was present in all cases. Masses of pyothorax-associated lymphoma were commonly located in the lateral costal pleura (50%) or at the costophrenic angle (30%). The tumor matrix often appeared heterogeneous and contained areas of necrosis (60%). Direct invasion of the chest wall, ribs, lung parenchyma, and abdomen was found in 75%, 50%, 25%, and 25% of patients. Gallium scans, when available, showed marked uptake in 10 of 13 patients (76.9%).

CONCLUSION. In patients who have undergone artificial pneumothorax therapy for tuberculosis more than 20 years in the past, a pleural soft-tissue mass adjacent to the margin of a coexistent empyema cavity suggests the presence of pyothorax-associated lymphoma. Knowledge of the typical radiologic findings and locations of pyothorax-associated lymphoma help in the diagnosis of this rare pathologic entity.

Keywords: CT, empyema, pleura, pyothorax-associated lymphoma, tumors

DOI:10.2214/AJR.09.2603

Received February 19, 2009; accepted after revision July 12, 2009.

[1]Department of Radiology, Stanford University School of Medicine, 300 Pasteur Dr., Rm. S-072, Stanford, CA 94305. Address correspondence to T. Ueda (takueda-rad@umin.ac.jp).

[2]National Cancer Center Hospital, Tokyo, Japan.

[3]Nagano PET and Diagnostic Center, Nagano, Japan.

[4]Department of Radiology, Numazu City Hospital, Shizuoka, Japan.

[5]Department of Radiology, Graduate School of Medicine, Chiba University, Japan.

AJR 2010; 194:76–84

0361–803X/10/1941–76

Pyothorax-associated lymphoma is a rare type of lymphoma that typically occurs in patients who have undergone artificial pneumothorax therapy for tuberculosis [1–4]. Results of several studies [1–4] have suggested that the development of pyothorax-associated lymphoma is triggered by long-standing empyema, that is, lasting for more than 20 years after the initial pneumothorax treatment. Until approximately 1970, artificial pneumothorax therapy for tuberculosis was performed mainly on younger patients. This treatment was gradually replaced by clinically more effective chemotherapy. A long latency period between the artificial pneumothorax treatment and the development of pyothorax-associated lymphoma, sometimes more than 40 years, has been reported [1–4]. Nakatsuka et al. [2] reported that 98 of 106 patients (92%) with pyothorax-associated lymphoma had a history of artificial pneumothorax therapy. Narimatsu et al. [4] reported that 78 of 98 patients (80%) had a similar history.

According to the literature, the mean age at diagnosis of pyothorax-associated lymphoma is approximately 60 years, and there is a predilection for men [1–4]. Common symptoms include chest pain, fever, and a palpable chest wall mass, which occur in approximately one half of patients. Respiratory symptoms such as productive cough, hemoptysis, and dyspnea are found in one fourth of patients [1, 2, 4]. Aozasa [5] reported a 2% incidence of pyothorax-associated lymphoma among patients with concomitant chronic empyema. The current pathophysiologic understanding of the disease suggests that both chronic Epstein-Barr virus (EBV) infection and an immunocom-

promised condition from long-standing chronic inflammation due to chronic empyema may be the causative mechanism of development of pyothorax-associated lymphoma [6, 7]. The histopathologic appearance of pyothorax-associated lymphoma is a soft-tissue mass arising from the thickened pleura and diffusely invading the parietal and visceral pleura. The pleura exhibits marked fibrous thickening with nonneoplastic inflammatory cells [1–3].

The prevalence of pyothorax-associated lymphoma is higher in Asia, especially Japan, than it is elsewhere [1–4, 8, 9]. There are two explanations for the higher prevalence in Japan. First, management of tuberculosis with artificial pneumothorax has been performed mainly in Asia, especially Japan [10]. Second, Epstein-Barr virus infection appears to have a higher incidence in Asia than in other areas [11, 12]. A few case reports [13–15] of pyothorax-associated lymphoma in Western countries have appeared. Pyothorax-associated lymphoma has been recognized worldwide as a specific entity owing to its listing in the 2004 World Health Organization classification of tumors [16]. Although the clinicopathologic features of pyothorax-associated lymphoma have been described and seem to be established in the literature, few studies have addressed the specific radiologic findings associated with this lesion [8, 9, 17–19]. The purpose of our study was to retrospectively analyze specific radiologic findings associated with pyothorax-associated lymphoma and to illustrate the spectrum of findings on chest radiographs, CT scans, and gallium scans.

Materials and Methods

Patient Selection

The cases of 21 patients (17 men, four women; median age, 71 years; range 52–77 years) with histopathologically proven pyothorax-associated lymphoma were retrospectively identified at seven Japanese medical centers. Digital databases, including the radiology information system, radiotherapy databases, and pathologic databases, of the institutions were searched for the period April 1985 to December 2008. This retrospective study was approved by our institutional review board with waiver of informed consent.

Clinical, histopathologic, and radiologic findings were reviewed. Chest radiographs and chest CT data were available for all patients. Eighteen of 21 CT examinations were performed with IV contrast administration. Slice thickness was 6–10 mm, and the reconstruction intervals were 5–10 mm. The tube current–time product ranged from 200 to 240 mAs, and the tube voltage was 120 kV. Whole-body ^{67}Ga scans were available for 13 patients. All ^{67}Ga scans were performed 72 hours after injection of 74 MBq ^{67}Ga-citrate. Whole-body imaging was performed in the anterior and posterior views, and spot camera images were obtained.

Imaging Findings

Two board-certified radiologists (9 and 10 years of experience in thoracic radiology) who were aware of the diagnosis of pyothorax-associated lymphoma reviewed images from all radiologic examinations in consensus.

Chest radiography—Chest radiographs were evaluated for the following imaging features: presence of extrapulmonary opacity associated with existing abnormalities from empyema, type of pleural calcification (circumferential, clusters on either the medially deviated visceral pleura or the lateral parietal pleura, or none), chest wall abnormalities (bulging soft-tissue mass along the lateral chest wall, soft-tissue opacity with loss of subcutaneous fat planes), air–fluid level formation in the empyema cavity, and bony destruction. Frontal view chest radiographs were reviewed in all cases and were complemented by a lateral image if available.

CT—Chest CT images were analyzed for the presence of empyema, soft-tissue masses, local extension of the masses, and distant extension (Fig. 1). The analysis of empyema included the following: shape of empyema cavity (oval, lenticular, or crescentic), pattern of pleural calcification (circumferential or partial), and presence of fistula formation (air–fluid level or air bubble in the empyema cavity). The CT criterion of a thickened and contrast-enhancing pleural layer (split pleura sign) enclosing a lenticular fluid collection was indicative of the presence of empyema. Analysis of aspirated pleural fluid and serologic tests were used to confirm the CT findings. The evaluation of a soft-tissue mass included location, shape (oval, lenticular, crescentic, lobulated), size (long- and short-axis measurements), relation to the coexistent empyema, and content. The locations of the soft-tissue mass were subclassified into the following five groups: lateral costal pleura, diaphragmatic pleura, apical pleura, pleura at the costophrenic angle, and mediastinal pleura. The relation between the soft-tissue mass and the coexistent empyema was categorized into the following three types: corner (center of the mass located eccentrically along the pleura adjacent to the margin of the empyema cavity), central (center of the mass located on the pleura next to the center of the empyema cavity), and remote (mass in no anatomic relation to the empyema cavity). The inner contents of the mass were categorized into homogeneous and heterogeneous enhancement; the latter was subdivided into necrotic and multilocular areas within the mass. We did not evaluate the absolute degree of mass enhancement because different contrast protocols were used at the various imaging centers. In the absence of IV contrast enhancement, the content was judged according to the density of the mass. Finally, the growth patterns of the masses were determined as predominantly external, symmetric, or internal growth tendency. External growth tendency was considered present when two thirds of the tumor mass was outside the pleural boundary (chest wall). Internal

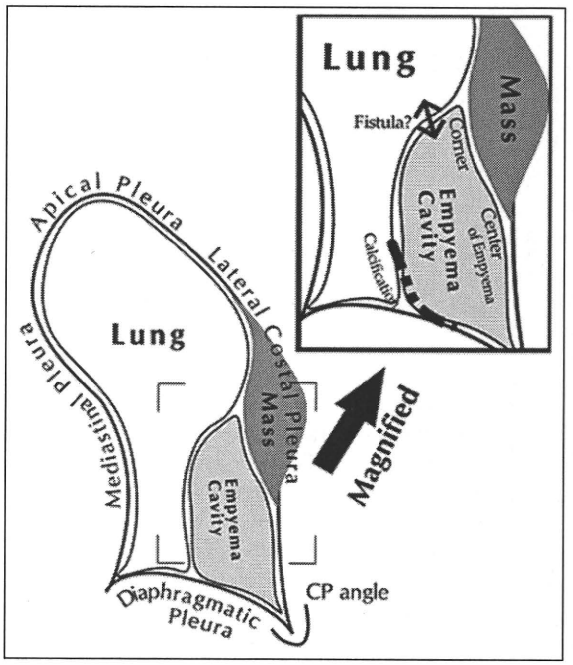

Fig. 1—Schematic shows CT features evaluated for characterization of empyema cavity (shape, pleural calcification, fistula formation) and soft-tissue mass (pyothorax-associated lymphoma) for location in relation to preexisting empyema (margin, central, or remote), shape, size, and content. Local extension of pyothorax-associated lymphoma (growth pattern, local or adjacent involvement, fistula formation) also is determined. CP = costophrenic.

growth tendency was the opposite, and symmetric growth was defined as that between external and internal growth.

The site of direct invasion of adjacent structures, including chest wall, rib, lung, abdomen, neck, mediastinum, pericardium, and spine, was recorded. Chest wall invasion was considered present when tumor was detected outside the ribs. Rib involvement was classified as osteolytic or osteoblastic. Extension into the lung was defined as masslike invasion of the lung parenchyma.

Gallium scanning—Abnormal uptake of ^{67}Ga-citrate was determined as follows: strong uptake (uptake of soft-tissue mass equal to or greater than that of liver parenchyma), moderate uptake (uptake of mass less than that of liver parenchyma), and weak uptake (uptake less than that of lung parenchyma). Distant involvement of pyothorax-associated lymphoma was considered the presence of abnormal uptake on the gallium scan and abnormal findings on CT images. Involvement of local lymph nodes or other distant organs was based on CT evidence of involvement and abnormal gallium accumulation if gallium imaging had been performed. A short-axis diameter measurement of 1.5 cm with strong ^{67}Ga-citrate uptake was defined as a positive finding of lymph node involvement.

Results

Clinicopathologic Findings

The clinicopathologic features of the patients are summarized in Table 1. In all cases, a histopathologic diagnosis of pyothorax-associated lymphoma was made with biopsy of the tumor. A history of artificial pneumothorax for management of tuberculosis and subsequent empyema was confirmed in the cases of 16 of the 21 patients. One patient had a history of long-standing empyema due to trauma from a traffic accident without a history of tuberculosis. Four patients did not have detailed information about the cause of chronic empyema. The median interval from the onset of empyema to the diagnosis of pyothorax-associated lymphoma was 45 years (range, 31–52 years). The symptoms at onset were chest wall pain in 14 patients, palpable chest wall mass in 12 patients, productive cough in five patients, dyspnea in three patients, and fever with weight loss in three patients. One patient had Horner syndrome [20].

The histopathologic subtypes of pyothorax-associated lymphoma included diffuse large B-cell lymphoma in 19 patients (90.5%) and peripheral T-cell lymphoma in two patients (9.5%). Results of laboratory testing for accompanying EBV infection were available

TABLE 1: Clinicopathologic Features of Pyothorax-Associated Lymphoma (n = 21)

Feature	Value
Age at diagnosis (y)	
Median	71
Range	52–77
Sex (no.)	
Men	17
Women	4
Male/female ratio	4.3/1
History of pyothorax (no.)	
Artificial pneumothorax for tuberculosis therapy	16 (76.2)
Traffic accident	1 (4.8)
Other	4 (19.0)
Latency from tuberculosis therapy to diagnosis of pyothorax-associated lymphoma (y)	
Median	45
Range	31–52
Symptom at diagnosis of pyothorax-associated lymphoma (no.)	
Chest pain	14 (66.7)
Chest wall mass	12 (57.1)
Productive cough	5 (23.8)
Dyspnea	3 (14.3)
Fever, weight loss	3 (14.3)
Horner syndrome	1 (4.8)
Histopathologic type (no.)	
Diffuse large B cell type	19 (90.5)
Peripheral T cell type	2 (9.5)
Epstein-Barr virus infection result (no.) (n = 8)	
Positive	7 (87.5)
Negative	1 (12.5)
Unavailable	13
Treatment (no.)	
Chemotherapy	4 (19.0)
Radiation therapy	4 (19.0)
Chemotherapy and radiation therapy	9 (42.9)
No therapy	1 (4.8)
Unknown	3 (14.3)
Outcome (no.)	
Death of pyothorax-associated lymphoma	13 (61.9)
Death of other cause	1 (4.8)
Alive with recurrence	1 (4.8)
Alive without recurrence	3 (14.3)
Unknown	3 (14.3)
Survival period after diagnosis (mo)	
Mean	22
Range	2–98

Note—Values in parentheses are percentages.

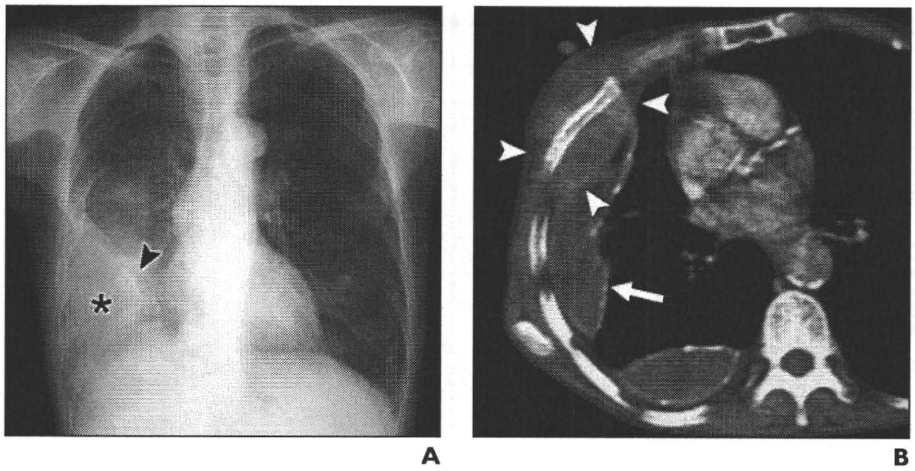

Fig. 2—65-year-old woman with pyothorax-associated lymphoma and history of therapy for tuberculous pleuritis 52 years previously.
A, Chest radiograph shows opaque extrapulmonary mass (*asterisk*) in right thoracic cavity. Visceral pleura is medially deviated with linear calcification (*arrowhead*).
B, Contrast-enhanced CT scan shows two chronic empyema cavities with partial calcification (*arrow*) and lenticular soft-tissue mass (*arrowheads*) symmetrically extending across lateral pleura eccentrically at margin of empyema cavity. Mass exhibits moderate enhancement compared with empyema cavity.

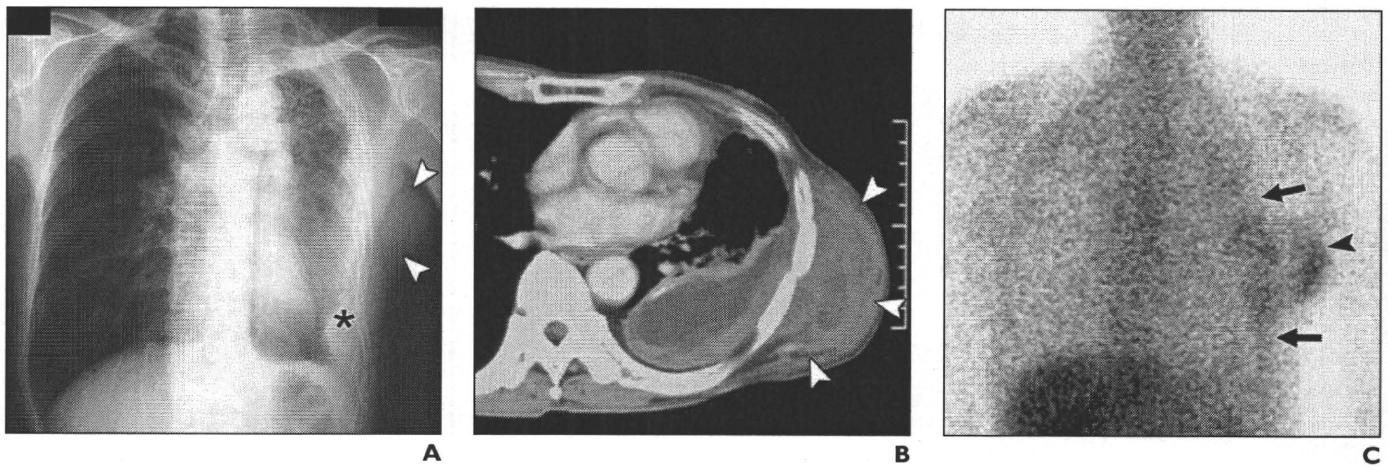

Fig. 3—72-year-old man with pyothorax-associated lymphoma and 40-year history of tuberculous empyema.
A, Chest radiograph shows diffuse pleural thickening with extrapulmonary opacity (*asterisk*) in left thoracic cavity and bulging mass on lateral chest wall (*arrowheads*).
B, Contrast-enhanced CT scan shows crescent-shaped mass on chest wall (*arrowheads*). Necrotic mass dominantly extends outside lateral pleura adjacent to lenticular empyema cavity.
C, Gallium scan shows moderate accumulation corresponding to soft-tissue mass (*arrowhead*). Tail of accumulation extends along pleura (*arrows*). No accumulation is present in empyema cavity.

for eight patients; seven of the eight patients (87.5%) had positive results for EBV.

Four of the patients with pyothorax-associated lymphoma were treated with chemotherapy; four, radiation therapy; and nine patients, combined chemotherapy and radiation therapy. One patient underwent no treatment, and three patients had no record of treatment and outcome. Thirteen of 21 patients (61.9%) died of pyothorax-associated lymphoma a mean of 22 months (range, 2–98 months) after the diagnosis was made.

Radiographic Features

The findings of pyothorax-associated lymphoma on chest radiographs are summarized in Table 2. An extrapulmonary opacity within the thoracic cavity corresponding to the CT finding of an empyema cavity was found in all patients (Figs. 2 and 3). Pleural calcifications were common (76%) and predominately involved the visceral pleura, which was medially deviated by the empyema cavity (Figs. 2, 4, and 5). Chest wall abnormalities were found in 15 patients (71.4%). One third of the patients had bulging soft-tissue masses on the lateral chest wall (Figs. 3 and 4), and one third of patients had soft-tissue opacities with loss of fat plane along the chest wall without having a mass effect. Air–fluid levels in the empyema cavity were identified in three patients (14.3%) (Fig. 4). Bony destruction was detected in four patients (19.0%) (Fig. 4).

CT Features

Table 3 shows the CT findings in each patient with regard to the coexistent empyema cavity, soft-tissue mass of pyothorax-associat-

TABLE 2: Chest Radiographic Findings of Pyothorax-Associated Lymphoma (*n* = 21)

Finding	No.
Intrathoracic extrapulmonary mass	21 (100)
Calcification of pleura	
Circular	3 (14.3)
Partial	13 (61.9)
None	5 (23.8)
Chest wall abnormality	15 (71.4)
Bulging chest wall soft-tissue mass	8 (38.1)
Soft-tissue opacity without mass effect	7 (33.3)
Air–fluid level in empyema cavity	3 (14.3)
Bone destruction	4 (19.0)

Note—Values in parentheses are percentages.

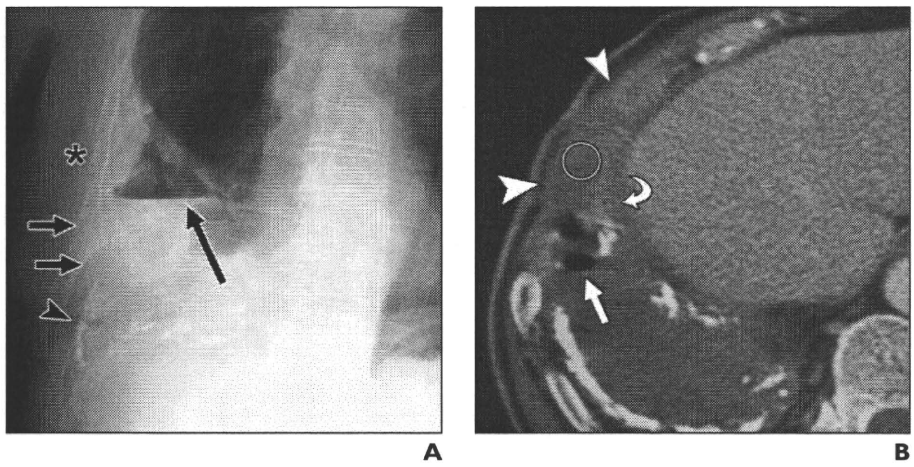

Fig. 4—71-year-old man with fistula formation between lung and empyema cavity due to invasion by pyothorax-associated lymphoma.
A, Chest radiograph shows air–fluid level in empyema cavity (*long arrow*). Thick calcification (*arrowhead*) in costophrenic angle is deviated medially by soft-tissue opacity straddling costophrenic angle. Anterior portions of right sixth and seventh ribs are destroyed by mass (*short arrows*). Asterisk indicates extrapulmonary mass with chest wall invasion.
B, Contrast-enhanced CT image shows empyema cavity with thick capsular calcification and crescentic soft-tissue mass (*arrowheads*) in costophrenic angle. Mass invades capsule of empyema cavity (*curved arrow*) to form air–fluid levels in cavity (*straight arrow*). Anterior portion of sixth rib is destroyed by tumor invasion (*circle*).

ed lymphoma, and the features of local extension. The cumulative results also are shown. Coexistent empyema was recognized in all 21 patients as an encapsulated cavitary lesion (Figs. 2–4). The shape of the empyema cavity was oval in nine patients (42.9%), crescentic in seven patients (33.3%), and lenticular in five patients (23.8%). Pleural calcifications associated with empyema were present in all patients; five patients (23.8%) had circular calcification, and 16 (76.2%) had partial calcification of the empyema sac (Figs. 2 and 3). Fistula formation with an air–fluid level or air bubble in the empyema cavity had occurred in eight patients (38.1%) (Fig. 4).

Soft-tissue masses adjacent to the empyema were depicted in 20 patients (Figs. 2–5). One patient had no soft-tissue mass, and the diagnosis was made only at cytologic examination of aspirate from the empyema cavity. Ten pyothorax-associated lymphoma masses (50%) were located on the lateral pleura (Figs. 2 and 3), and seven (33%) straddled the costophrenic angle (Fig. 4). The others were on the apical pleura (10.0%), diaphragmatic pleura (5.0%) (Fig. 5), or mediastinal pleura (5.0%). All masses were adjacent to the coexistent empyema corner (Figs. 2–5). The soft-tissue mass was lenticular in 12 patients (60.0%) (Fig. 2), crescentic in four patients

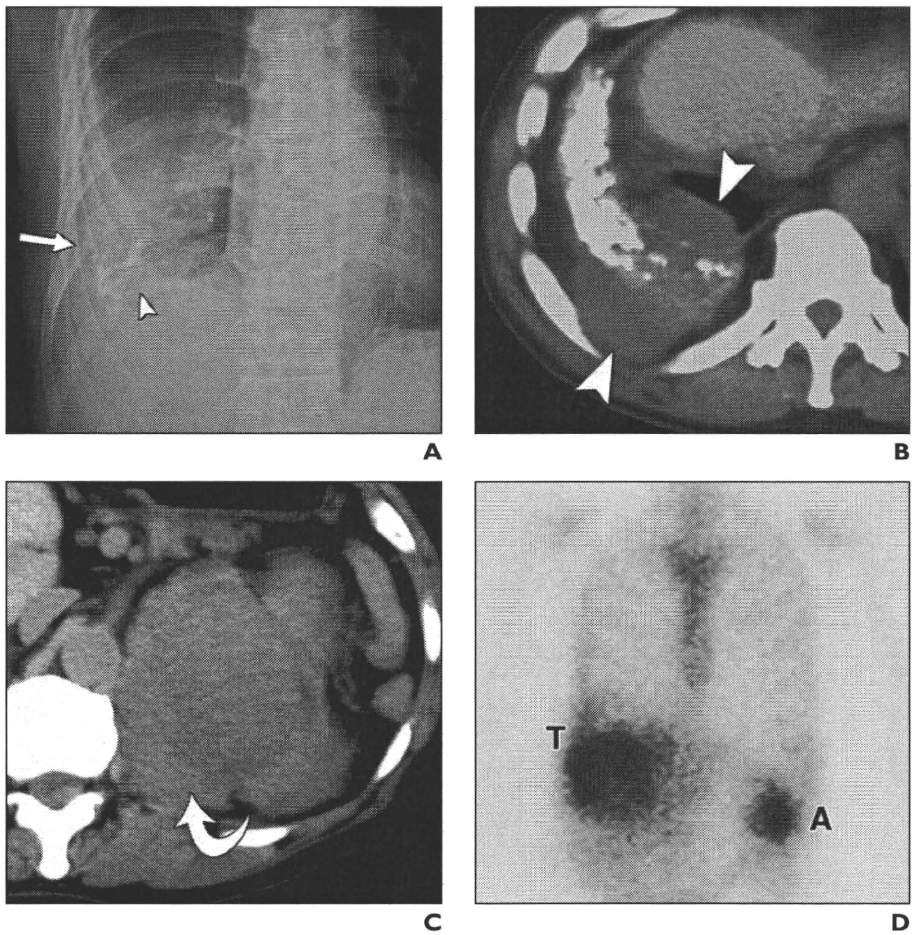

Fig. 5—71-year-old man with pyothorax-associated lymphoma with direct invasion through right diaphragm into abdomen and distant involvement of left adrenal gland (patient 2).
A, Chest radiograph shows soft-tissue opacity (*arrow*) in right lower thoracic cavity overlying calcified diaphragm (*arrowhead*).
B, Unenhanced CT scan shows ovoid soft-tissue mass overlying calcified diaphragmatic pleura extending through diaphragm into peritoneal cavity (*arrowheads*).
C, Unenhanced CT scan at lower level than **B** shows left adrenal soft-tissue mass (*arrow*).
D, Gallium scintigram shows marked tracer accumulation in both chest wall mass (T) and left adrenal mass (A).

TABLE 3: CT Findings of Pyothorax-Associated Lymphoma

Patient No.	Empyema			Soft-Tissue Mass					Local Extension						Distant Involvement
	Shape	Calcification	Fistula	Location	Relation to Empyema	Shape	Size (mm)	Content	Growth Pattern	Chest Wall	Rib	Lung	Abdomen	Other	
1	Lenticular	Partial	Absent	Lateral costal pleura	Corner	Lenticular	62 × 28	Necrotic	Symmetric	Present	Osteolytic invasion	Absent	Absent		
2	Crescent	Partial	Absent	Diaphragmatic pleura	Corner	Oval	59 × 45	Homogeneous	Symmetric	Absent	Absent	Absent	Present		Adrenal gland
3	Lenticular	Partial	Present	Lateral costal pleura	Corner	Lenticular	177 × 71	Necrotic	External	Present	Osteolytic invasion	Absent	Absent	Scapula	
4	Lenticular	Partial	Absent	Lateral costal pleura	Corner	Lobulated	81 × 49	Multilocular	External	Present	Osteolytic invasion	Absent	Absent		
5	Lenticular	Partial	Absent	Lateral costal pleura	Corner	Crescent	125 × 84	Necrotic	External	Present	Osteoblastic invasion	Absent	Absent		
6	Oval	Partial	Absent	Lateral costal pleura	Corner	Lenticular	33 × 21	Necrotic	Symmetric	Absent	Absent	Absent	Absent		
7	Lenticular	Circular	Absent	Apical pleura	Corner	Oval	72 × 61	Homogeneous	External	Absent	Osteoblastic invasion	Absent	Absent	Neck	
8	Oval	Circular	Present	Lateral costal pleura	Corner	Lenticular	59 × 40	Homogeneous	Internal	Present	Osteolytic invasion	Absent	Absent		
9	Crescent	Partial	Present	Pleura at costophrenic angle	Corner	Lenticular	118 × 73	Multilocular	External	Present	Osteolytic invasion	Present	Present		
10	Oval	Partial	Absent	Lateral costal pleura	Corner	Lenticular	33 × 20	Homogeneous	Symmetric	Present	Absent	Present	Absent		
11	Crescent	Partial	Present	Lateral costal pleura	Corner	Lenticular	204 × 155	Necrotic	Symmetric	Present	Absent	Present	Present	Mediastinum, vertebra	
12	Crescent	Circular	Present	Pleura at costophrenic angle	Corner	Crescent	75 × 21	Necrotic	Symmetric	Present	Osteolytic invasion	Present	Absent		
13	Oval	Partial	Absent	Lateral costal pleura	Corner	Crescent	125 × 61	Necrotic	External	Present	Osteolytic invasion	Absent	Absent		Adrenal gland
14	Oval	Partial	Absent	Pleura at costophrenic angle	Corner	Lenticular	44 × 32	Homogeneous	Symmetric	Absent	Absent	Absent	Absent		
15	Oval	Partial	Present	Mediastinal pleura	Corner	Lenticular	56 × 45	Necrotic	Symmetric	Present	Absent	Absent	Absent		Thoracic lymph nodes
16	Crescent	Partial	Absent	Pleura at costophrenic angle	Corner	Lenticular	74 × 44	Necrotic	External	Present	Osteolytic invasion	Absent	Present		

(Table 3 continues on next page)

TABLE 3: CT Findings of Pyothorax-Associated Lymphoma (continued)

Patient No.	Empyema			Soft-Tissue Mass					Local Extension					Distant Involvement
	Shape	Calcification	Fistula	Location	Relation to Empyema	Shape	Size (mm)	Content	Growth Pattern	Chest Wall	Rib	Lung	Abdomen	Other	
17	Crescent	Partial	Present	Pleura at costophrenic angle	Corner	Lenticular	64 × 43	Necrotic	Symmetric	Present	Osteolytic invasion	Present	Absent		Kidneys
18	Oval	Circular	Absent	No tumor detected; lymphoma proved with cytologic examination											
19	Oval	Circular	Absent	Apical pleura	Corner	Lobulated	70 × 58	Multilocular	External	Absent	Osteoblastic invasion	Absent	Absent	Neck	
20	Oval	Partial	Absent	Lateral costal pleura	Corner	Lenticular	65 × 55	Necrotic	Symmetric	Present	Absent	Absent	Absent		
21	Crescent	Partial	Present	Pleura at costophrenic angle	Corner	Crescent	88 × 53	Necrotic	Symmetric	Present	Osteolytic invasion	Absent	Present		Thoracic and abdominal lymph nodes
Cumulative result (%)	Oval, 42.9 Crescent, 33.3 Lenticular, 23.8	Partial, 76.2 Circular, 23.8 None, 0.0	Present, 38.1 Absent, 61.9	Lateral costal pleura, 50.0 Pleura at costophrenic angle, 30.0 Apical pleura, 10.0 Diaphragmatic pleura, 5.0 Mediastinal pleura, 50.0	Corner, 100.0 Central, 0.0 Remote, 0.0	Lenticular, 60.0 Crescent, 20.0 Oval, 10.0 Lobulated, 10.0	Mean, 84.2 × 53 SD, 44.8 × 29.9	Necrotic, 15.0 Homogeneous, 60.0 Multilocular, 25.0	Symmetric, 5.0 External, 55.0 Internal, 40.0	Present, 75.0 Absent, 25.0	Osteolytic invasion, 50.0 Osteoblastic invasion, 15.0 Absent, 35.0	Present, 25.0 Absent, 75.0	Present, 25.0 Absent, 75.0		

(20.0%) (Fig. 3), oval in two patients (10.0%) (Fig. 5), and lobulated in two patients (10.0%). The mean long- and short-axis measurements were 84.2 mm (range, 33–204 mm) and 53.0 mm (range, 20–155 mm). The content of the masses was homogeneous (Fig. 5) in five patients (15.0%), necrotic (Fig. 4) in 12 patients (60.0%), and multilocular in two patients (10.0%).

Eleven of 20 soft-tissue masses exhibited symmetric expansile growth along the pleura (Fig. 2). Eight masses (40.0%) had external-dominant extension outside the thoracic cavity (Fig. 3). Only one mass (5.0%) had internal-dominant extension. Chest wall invasion was common, being detected in 15 patients (75.0%) (Figs. 2 and 3). Rib involvement was found in 13 patients (65.0%), and osteolytic lesions (Fig. 4) were more common (50.0%) than osteoblastic lesions (15.0%). Other sites of direct invasion included the lung parenchyma in five patients (25.0%); abdomen through the diaphragm (Fig. 5) in five patients (25.0%); cervical soft tissues in two patients (10.0%); scapula in one patient (5.0%); and mediastinum, pericardium, and vertebra in one patient (5.0%).

Gallium Scanning

Among 13 patients for whom gallium scans were available, 10 patients (76.9%) had marked gallium accumulation in the soft-tissue masses (Figs. 3 and 5). Two patients had moderate accumulation, and one patient had weak accumulation.

Distant Involvement

Lymph node involvement was found in two patients. One of these patients had intrathoracic lymph node involvement, and the other had intrathoracic and extrathoracic lymph node involvement. Distant involvement was detected in three patients. Two patients had adrenal involvement (Fig. 5), and one patient had bilateral renal involvement. The three patients with distant involvement had no lymph node involvement.

Discussion

Pyothorax-associated lymphoma is a rare disease with variations in endemic prevalence [3]. Although there have been many reports from Asia [8, 9], especially Japan [2, 4], there have been only a few reports from Western countries [13–15]. Pyothorax-associated lymphoma therefore has not been fully recognized on a global scale. As details about the pathogenesis and cellular origin have been revealed through clinicopathologic and immunohistologic studies [7], pyothorax-associated lymphoma has been recognized as a specific type of lymphoma. The disease was listed in the World Health Organization classification in 2004 [16]. In that document it is described as "a rare type of non-Hodgkin's lymphoma of exclusively B-cell phenotype occurring in patients with a clinical history of longstanding pyothorax resulting from pulmonary tuberculosis or tuberculous pleuritis, strongly associated with Epstein-Barr virus infection."

It is important to recognize the presence of pyothorax-associated lymphoma because it is a malignant, life-threatening condition with a much poorer prognosis than the benign chronic empyema. The growing trend of globalization increases the possibility of encountering this exceptional disease throughout the world, including Western countries. Radiologists should be aware of this rare but malignant disease because early detection is key to successful treatment [21].

Although many investigators have described the pathogenesis and histopathologic features of pyothorax-associated lymphoma, only a

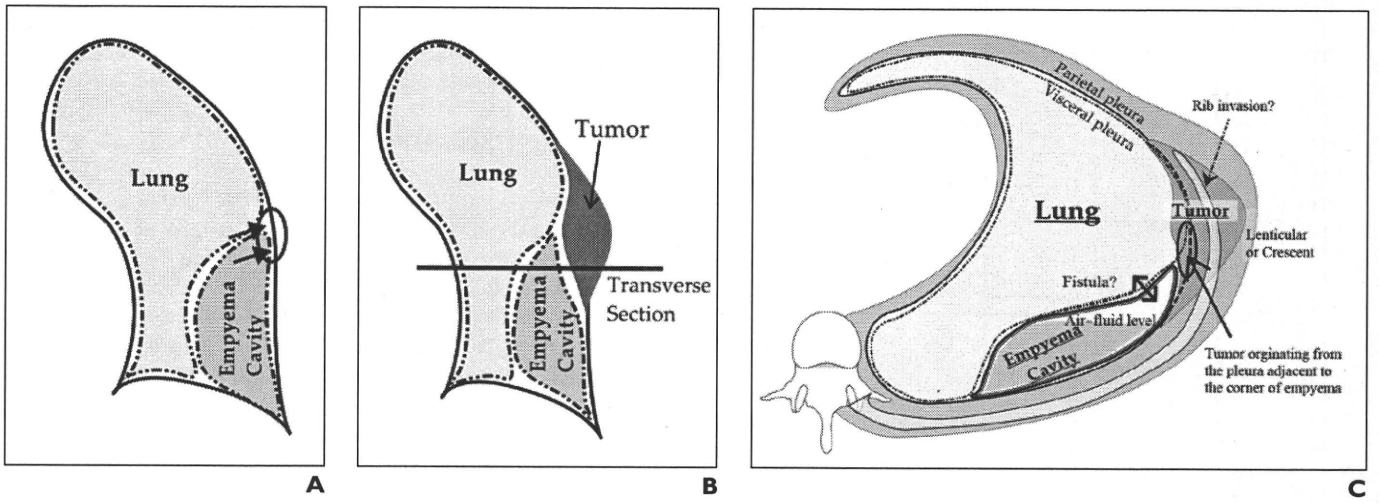

Fig. 6—Development and typical CT findings of pyothorax-associated lymphoma.
A, Schematic shows that after artificial pneumothorax in management of pulmonary tuberculosis or tuberculous pleuritis, chronic empyema can develop in intrathoracic extrapleural space. Pleura adjacent to empyema cavity is constantly stimulated by chronic inflammation, and it is thought that chronic Epstein-Barr virus infection may be associated with tumorigenesis of pyothorax-associated lymphoma.
B, Schematic shows pyothorax-associated lymphoma developing more than 20 years after therapy for tuberculosis in association with immunocompromised condition due to long-standing inflammation.
C, Schematic shows typical CT features include soft-tissue mass commonly located on lateral pleura eccentrically at margin of empyema cavity. Shape of mass is commonly lenticular or crescentic. Symmetric or external extension to thoracic cavity is common. Air–fluid level in empyema cavity may be present when tumor extends to empyema capsule to form fistula. Mass frequently invades chest wall and ribs.

few reports have elaborated specific radiologic findings [9, 17]. We found typical radiologic findings of pyothorax-associated lymphoma that reflect its pathogenesis and histopathologic characteristics (Fig. 6). It seems likely that chronic stimulation by the long-standing presence of empyema favors development of neoplasia in the pleura [3].

Pyothorax-associated lymphoma commonly demonstrates a lenticular or crescent-shaped soft-tissue mass straddling the thickened pleura at the margin of a coexistent empyema cavity (Fig. 6). The lesion has a tendency to invade adjacent structures, the exact structures depending on the anatomic location of the empyema. Frequent sites of invasion are the chest wall, rib, and lung when the tumor is located on the lateral costal pleura. A less frequent site is the abdomen through the diaphragm when the empyema is in the costophrenic angle or along the diaphragm. CT frequently depicts air–fluid levels or air bubble formation in the empyema cavity, and these signs may be associated with fistula formation caused by the tumor invasion. Fistula formation also can occur in chronic empyema without a tumor but is not common [22]. In our series, 60% of lesions exhibited heterogeneity of the mass compatible with areas of necrosis, which is uncommon in the other types of non-Hodgkin's lymphoma [23]. Previous authors [1, 2, 4] have reported distant involvement of pyothorax-associated lymphoma, including the cervical, mediastinal, and abdominal lymph nodes; superficial lymph nodes; adrenal glands; liver; stomach; kidneys; CNS; spleen; small intestine; and pancreas. Lymph node involvement was found in only 10% of patients in our study, and distant involvement of the adrenal glands or kidneys occurred in only 15% of patients.

The most important differential diagnoses of pyothorax-associated lymphoma are benign complications of chronic empyema. Aggressive features at reactivation of tuberculosis can mimic the occurrence of tumors. Among them, tuberculous empyema necessitatis, defined as subcutaneous abscess formation through the parietal pleura into the chest wall, is one of the most important differential diagnoses of pyothorax-associated lymphoma [8, 9]. Although previous studies have shown difficulties in differentiation of malignant tumors and benign chronic empyema, the typical findings of pyothorax-associated lymphoma in our study seem to be pathognomonic, or, at least, they help to increase the sensitivity of detection of this rare malignant disease. Our results suggest that the soft-tissue component of pyothorax-associated lymphoma can be differentiated from the coexisting empyema. Even though this disease is rare and can be difficult to diagnose with imaging alone, knowledge of the typical location of pyothorax-associated lymphoma—eccentrically at the margin of the empyema cavity—should lead to the optimal location for tissue sampling when biopsy of the mass is planned [19].

Rare empyema-associated malignant tumors and malignant tumors accompanied by empyema to be considered in the differential diagnosis of pyothorax-associated lymphoma include mesothelioma, angiosarcoma, malignant fibrous histiocytoma, and squamous cell carcinoma [9, 17, 24–28]. Malignant pleural mesothelioma and empyema can coexist, but a correlation between these two diseases has not been specifically reported, to our knowledge. Malignant pleural mesothelioma commonly extends along the pleural cavity, and the pleura-based mass tends to spread diffusely throughout the thoracic cavity. Focal and localized mesotheliomas are rather rare tumors but are thought to be similar to pyothorax-associated lymphoma [24]. A history of asbestos exposure appears helpful for differentiating mesothelioma from pyothorax-associated lymphoma [24]. Rare cases of malignant fibrous histiocytoma, angiosarcoma, and squamous cell carcinoma or sarcoma in association with tuberculous pyothorax have been described, but few data appear in the literature with regard to the specific radiologic manifestations [25, 26]. Specific imaging features of pyothorax-associated lymphoma, such as symmetric growth pattern of a mass at the margin of chronic empyema,

therefore appear to be distinct from other empyema-associated malignant lesions.

Our study had limitations. We performed a retrospective data analysis of cases of pyothorax-associated lymphoma collected from several institutions. Although the number of cases seems small, our study exceeded other descriptions of the imaging features of this rare disease. Furthermore, we could not control the heterogeneity of CT parameters among the different institutions. Finally, we did not specifically analyze differences between patients with pyothorax-associated lymphoma and patients with benign chronic empyema or compare the findings of pyothorax-associated lymphoma with those of other empyema-associated malignant lesions, which appear to be even less common [9].

Many reports have shown the utility of gallium scans in the diagnosis and assessment of response to therapy for lymphoma, including one report of pyothorax-associated lymphoma [21, 29]. Furthermore, ^{18}F-FDG PET has been routinely used for staging and monitoring of therapeutic response in lymphoma and has proven utility superior to that of gallium scanning [30]. Asakura et al. [31] reported the usefulness of FDG PET in the staging and monitoring of pyothorax-associated lymphoma. We conclude that knowledge of the illustrated typical radiologic findings of pyothorax-associated lymphoma is helpful for detecting this rare but fatal empyema-associated malignant lesion.

Acknowledgment

We thank R. Hallett for assistance in preparing the manuscript.

References

1. Iuchi K, Ichimiya A, Akashi A, et al. Non-Hodgkin's lymphoma of the pleural cavity developing from long-standing pyothorax. *Cancer* 1987; 60:1771–1775
2. Nakatsuka S, Yao M, Hoshida Y, Yamamoto S, Iuchi K, Aozasa K. Pyothorax-associated lymphoma: a review of 106 cases. *J Clin Oncol* 2002; 20:4255–4260
3. Aozasa K. Pyothorax-associated lymphoma. *J Clin Exp Hematop* 2006; 46:5–10
4. Narimatsu H, Ota Y, Kami M, et al. Clinicopathological features of pyothorax-associated lymphoma; a retrospective survey involving 98 patients. *Ann Oncol* 2007; 18:122–128
5. Aozasa K. Pyothorax-associated lymphoma. *Int J Hematol* 1996; 65:9–16
6. Kanno H, Aozasa K. Mechanism for the development of pyothorax-associated lymphoma. *Pathol Int* 1998; 48:653–664
7. Takakuwa T, Tresnasari K, Rahadiani N, Miwa H, Daibata M, Aozasa K. Cell origin of pyothorax-associated lymphoma: a lymphoma strongly associated with Epstein-Barr virus infection. *Leukemia* 2008; 22:620–627
8. Kim Y, Lee SW, Choi HY, Im SA, Won T, Han WS. A case of pyothorax-associated lymphoma simulating empyema necessitatis. *Clin Imaging* 2003; 27:162–165
9. Lee HY, Goo JM, Lee HJ, Lee CH, Chun EJ, Im JG. The value of computed tomography for predicting empyema-associated malignancy. *J Comput Assist Tomogr* 2006; 30:453–459
10. Herzog H. History of tuberculosis. *Respiration* 1998; 65:5–15
11. de-Thé G, Day NE, Geser A, et al. Sero-epidemiology of the Epstein-Barr virus: preliminary analysis of an international study: a review. *IARC Sci Publ* 1975; 11:3–16
12. Takeuchi K, Tanaka Taya K, Kazuyama Y, et al. Prevalence of Epstein-Barr virus in Japan: trends and future prediction. *Pathol Int* 2006; 56:112–116
13. Androulaki A, Drakos E, Hatzianastassiou D, et al. Pyothorax-associated lymphoma (PAL): a western case with marked angiocentricity and review of the literature. *Histopathology* 2004; 44:69–76
14. Riehl G, Aubert A, Sandu C, Brichon PY. Malignant non-Hodgkin's lymphoma developing late after pneumonectomy. *Eur J Cardiothorac Surg* 2006; 30:948–949
15. Verghese ET, Amer KM, Addis BJ. Pyothorax-associated lymphoma: an unusual variant of an unusual tumour. *Histopathology* 2007; 51:131–133
16. Banks PM, Harris NL, Warnke RA, Gaulard P. Tumors of the pleura: pyothorax-associated lymphomas. In: Travis WD, Brambilla E, Muller-Hermelink HK, Harris CC, eds. *World Health Organization classification of tumours, pathology & genetics: tumours of the lung, pleura, thymus and heart*. Lyon, France: IARC Press, 2004:138–140
17. Minami M, Kawauchi N, Yoshikawa K, et al. Malignancy associated with chronic empyema: radiologic assessment. *Radiology* 1991; 178:417–423
18. Kinoshita T, Ishii K, Taira Y, Naganuma H. Malignant lymphoma arising from chronic tuberculous empyema: a case report. *Acta Radiol* 1997; 38:833–835
19. Brun V, Revel MP, Danel C, Fournier LS, Souilamas R, Frija G. Case report: pyothorax-associated lymphoma—diagnosis at percutaneous core biopsy with CT guidance. *AJR* 2003; 180:969–971
20. George A, Haydar AA, Adams WM. Imaging of Horner's syndrome. *Clin Radiol* 2008; 63:499–505
21. Aruga T, Itami J, Nakajima K, et al. Treatment for pyothorax-associated lymphoma. *Radiother Oncol* 2000; 56:59–63
22. Westcott JL, Volpe JP. Peripheral bronchopleural fistula: CT evaluation in 20 patients with pneumonia, empyema, or postoperative air leak. *Radiology* 1995; 196:175–181
23. Pombo F, Rodriguez E, Caruncho MV, Villalva C, Crespo C. CT attenuation values and enhancing characteristics of thoracoabdominal lymphomatous adenopathies. *J Comput Assist Tomogr* 1994; 18:59–62
24. Metintas M, Ucgun I, Elbek O, et al. Computed tomography features in malignant pleural mesothelioma and other commonly seen pleural diseases. *Eur J Radiol* 2002; 41:1–9
25. Aozasa K, Naka N, Tomita Y, et al. Angiosarcoma developing from chronic pyothorax. *Mod Pathol* 1994; 7:906–911
26. Hattori H. Epithelioid angiosarcoma arising in the tuberculous pyothorax: report of an autopsy case. *Arch Pathol Lab Med* 2001; 125:1477–1479
27. Takanami I, Imamura T, Morota N, Kodaira S. Malignant fibrous histiocytoma of the chest wall developing after pleuropneumonectomy performed for tuberculous pyothorax: report of an unusual case. *J Thorac Cardiovasc Surg* 1994; 108:395–396
28. Ruttner JR, Heinzl S. Squamous-cell carcinoma of the pleura. *Thorax* 1977; 32:497–500
29. McCaffrey JA, Rudders RA, Kahn PC, et al. Clinical usefulness of 67gallium scanning in the malignant lymphomas. *Am J Med* 1976; 60:523–530
30. Kostakoglu L, Goldsmith SJ. Fluorine-18 fluorodeoxyglucose positron emission tomography in the staging and follow-up of lymphoma: is it time to shift gears? *Eur J Nucl Med* 2000; 27:1564–1578
31. Asakura H, Togami T, Mitani M, et al. Usefulness of FDG-PET imaging for the radiotherapy treatment planning of pyothorax-associated lymphoma. *Ann Nucl Med* 2005; 19:725–728

Int. J. Radiation Oncology Biol. Phys., Vol. ■, No. ■, pp. 1–9, 2010

0360-3016/$ - see front matter

ELSEVIER

doi:10.1016/j.ijrobp.2010.09.012

BIOLOGY CONTRIBUTION

GENETIC VARIANTS OF *NPAT-ATM* AND *AURKA* ARE ASSOCIATED WITH AN EARLY ADVERSE REACTION IN THE GASTROINTESTINAL TRACT OF PATIENTS WITH CERVICAL CANCER TREATED WITH PELVIC RADIATION THERAPY

ATSUKO ISHIKAWA, B.S.,* TOMO SUGA, M.S.,* YOSHIMI SHOJI, B.S.,* SHINGO KATO, M.D., PH.D.,† TATSUYA OHNO, M.D., PH.D.,† HITOSHI ISHIKAWA, M.D., PH.D.,† SHINJI YOSHINAGA, PH.D.,‡ KIYOSHI OHARA, M.D., PH.D.,§ HISANORI ARIGA, M.D., PH.D.,¶ KUNINORI NOMURA, M.D., PH.D.,‖ YUTA SHIBAMOTO, M.D., PH.D.,** KEN-ICHI ISHIKAWA, PH.D.,* TAKASHI MORITAKE, M.D., PH.D.,* YUICHI MICHIKAWA, PH.D.,* MAYUMI IWAKAWA, M.D., PH.D.,* AND TAKASHI IMAI, PH.D.*

*RadGenomics Project, †Research Center Hospital for Charged Particle Therapy, ‡Research Center for Radiation Protection, National Institute of Radiological Sciences, Chiba; §Tsukuba University Hospital, Tsukuba; ¶Tohoku University Hospital, Miyagi; ‖Toyama University Hospital, Toyama; and **Nagoya City University Hospital, Aichi, Japan

Purpose: This study sought to associate polymorphisms in genes related to cell cycle regulation or genome maintenance with radiotherapy (RT)-induced an early adverse reaction (EAR) in patients with cervical cancer.
Methods and Materials: This study enrolled 243 cervical cancer patients who were treated with pelvic RT. An early gastrointestinal reaction was graded using the National Cancer Institute Common Toxicity Criteria, version 2. Clinical factors of the enrolled patients were analyzed, and 208 patients were grouped for genetic analysis according to their EAR (Grade ≤1, *n* = 150; Grade ≥2, n = 58). Genomic DNA was genotyped, and association with the risk of EAR for 44 functional single-nucleotide polymorphisms (SNPs) of 19 candidate genes was assessed by single-locus, haplotype, and multilocus analyses.
Results: Our analysis revealed two haplotypes to be associated with an increased risk of EAR. The first, comprising rs625120C, rs189037T, rs228589A, and rs183460G, is located between the 5' ends of *NPAT* and *ATM* (OR = 1.86; 95% CI, 1.21–2.87), whereas the second is located in the *AURKA* gene and comprises rs2273535A and rs1047972G (OR = 1.75; 95% CI, 1.10–2.78). A third haplotype, rs2273535T and rs1047972A in *AURKA*, was associated with a reduced EAR risk (OR = 0.42; 95% CI, 0.20–0.89). The risk of EAR was significantly higher among patients with both risk diplotypes than in those possessing the other diplotypes (OR = 3.24; 95% CI, 1.52–6.92).
Conclusions: Individual radiosensitivity of intestine may be determined by haplotypes in the *NPAT-ATM* and *AURKA* genes. These variants should be explored in larger association studies in cervical cancer patients.

Cervical cancer, Early adverse reaction, Haplotype, Radiosensitivity, Association study.

INTRODUCTION

Cancer patients experience individual variation in normal tissue reactions after radiotherapy (RT). Such reactions to RT are quite complex, with multiple genetic factors contributing to a patient's susceptibility for such adverse reactions to RT (1, 2). Identification of genetic markers associated with a risk of adverse reactions will facilitate the development of new procedures for protecting high-risk patients from the adverse reactions and will improve our understanding of the biologic mechanisms determining individual radiosensitivity.

Uterine cervical cancer (CC) is the second most common malignancy among women worldwide. The number of incident cases of CC in 2002 was approximately 493,000, and deaths resulting from CC numbered 274,000 (3). The

Reprint requests to: Takashi Imai, Ph.D., RadGenomics Project, National Institute of Radiological Sciences, Anagawa, 4-9-1, Inage, Chiba, 263-8555 Japan. Tel: (+81) 43-206-3138; Fax: (+81) 43-206-6267; E-mail: imait@nirs.go.jp

Atsuko Ishikawa and Tomo Suga contributed equally to this study.

Dr. Ohno's present address: Gunma University Faculty of Medicine, Gunma, Japan. Dr. Ohara's present address: Regional Cancer Center, Tsuchiura Kyodo General Hospital, Tsuchiura, Japan. Dr. Moritake's present address: Proton Medical Research Center, University of Tsukuba, Tsukuba, Japan.

Supplementary materials for this article can be found at www.redjournal.org

Conflict of interest: none.

Acknowledgment—The authors thank all the DNA donors and collaborating clinicians for their participation in this study, and Azusa Ohno, Saeko Takekawa, Keiko Ogawa, and Masayo Terada for supporting the data management.

Received June 21, 2010, and in revised form Aug 26, 2010. Accepted for publication Sept 1, 2010.

currently recommended therapeutic modality for locally advanced CC is concomitant chemotherapy and RT (4–8). The treatment volume of RT for CC involves several normal structures such as the small bowel, colon, rectum, and urinary bladder. Therefore, an early adverse reaction (EAR) of the intestinal tract is one of the major concerns in the treatment of CC. The risk of intestinal toxicity could be related to individual differences in radiosensitivities of the mitogenic crypt cells contained therein under present treatment protocols.

Approximately 60 studies have addressed possible associations between genetic sequence alterations and the risk of adverse reactions (2, 9, 10). Many of these focused on candidate genes involved in inflammatory response pathways such as *TGFB1*, DNA repair such as *XRCC1* and *XRCC3*, DNA damage signaling and cell cycle control such as *ATM*, and oxidative stress responses such as *SOD2*. Adverse reactions (AR) after RT were analyzed in patients with mainly breast and prostate tumors. Only one study, to our knowledge, has investigated associations between genetic alterations and AR in patients with gynecologic tumors, correlating single-nucleotide polymorphisms (SNPs) or microsatellite polymorphisms on *XRCC1*, *XRCC3, XRCC5, OGG1*, and *TGFB1* with the occurrence of late normal tissue reactions after RT (11–13).

We recently conducted an association study of early adverse skin reactions in breast cancer patients who underwent breast-conserving RT, and consequently suggested that haplotypes in *MAD2L2, PTTG1*, *RAD9A*, *LIG3,* and *CD44* are associated with such reactions in breast cancer patients (14). Based on these findings, we proposed that early skin reactions arise from damage to the self-renewing epidermal cells because four of the candidate genes function in cell cycle regulation and/or chromosome maintenance, involving sister chromatid separation and also the mitotic spindle checkpoint and damage sensor. We therefore hypothesized that gene variations likely to affect cell cycle regulation or genome maintenance could contribute to heterogeneity in the risk of adverse intestinal reactions in CC patients undergoing RT.

Our DNA typing system (14) classified 27 genes as related to cell cycle or genome maintenance according to the biologic categories of the Gene Ontology database (15). We selected 206 functional SNPs, coding SNP (cSNP) and regulatory SNP (rSNP), within or surrounding these 27 candidate genes in addition to the previously reported genes including *CD44*, *XRCC1*, *XRCC3, OGG1*, and *TGFB1* for analysis in this study.

METHODS AND MATERIALS

Study participants

A total of 243 uterine CC patients treated with pelvic RT were registered from 2001 to 2007 across five collaborating institutions in Japan: Research Center Hospital for Charged Particle Therapy National Institute of Radiological Sciences; Tsukuba University Hospital; Tohoku University Hospital; Toyama University Hospital; and Nagoya City University Hospital. The following eligibility criteria were used in the current survey: patients were required to have CC as their initial clinical diagnosis and to have been treated with whole pelvic RT. All study patients and 133 healthy donors provided written informed consent to participate in the study, which was approved by the Ethics Committee at the National Institute of Radiological Sciences and at each collaborating institution. All identified information was managed at the Medical Information Processing Office of the Research Center Hospital for Charged Particle Therapy of the National Institute of Radiological Sciences.

The National Cancer Institute Common Toxicity Criteria, version 2, was used to grade EARs of the intestinal tract, namely, frequency of stools/day, and need for parenteral support for dehydration that developed within 3 months after the initiation of RT. Definition of grade of diarrhea was as follows: Grade 0, none; Grade 1, increase of <4 stools/day over pretreatment; Grade 2, increase of 4–6 stools/day; Grade 3, increase of ≥7 stools/day or parenteral support for dehydration. Differences in clinical features such as age at RT, smoking habit, alcohol habit, pathologic diagnosis, International Federation of Gynecology and Obstetrics stage, and treatment modality (Table E1) among the grades of AR were assessed by p values using the Fisher exact (FE) test, the Kruskal-Wallis (KW)test, the Mann-Whitney U (MU)test, and the Cochran-Armitage (CA)test. A p value <0.05 was regarded as statistically significant.

Candidate genes and SNPs

A total of 27 cell cycle regulation or chromosome-maintenance genes were selected as candidates for this association study. From these, 182 functional SNPs, constituting cSNPs and rSNPs localized within the 3-kb region upstream from each transcription start site, were selected for analysis. Additionally, 24 SNPs in five genes, which were previously reported by us (*CD44*) (14) and by de Ruyck *et al.* (*TGFB1, XRCC1, XRCC3,* and *OGG1*) (11–13), were genotyped. Furthermore, 11 intron SNPs (iSNPs) within the *NPAT* and *ATM* genes, which are localized contiguously on chromosome 11q22–23, were selected for pairwise linkage disequilibrium (LD) analysis. Allele and genotype frequencies for each polymorphic marker were calculated, and nonpolymorphic or rare markers indicating less than 5% of the minor allele frequency in the CC patients were excluded from subsequent analyses.

Preparation of genomic DNA and genotyping using the MassARRAY system (Sequenome, San Diego, CA) was performed as previously described (14, 16).

Allele, genotype, haplotype, and diplotype analyses

Allele and genotype frequencies for each polymorphism were calculated, and the Hardy-Weinberg equilibrium was evaluated using the chi-square test among both healthy donors and the total cohort of CC patients. Statistical significance and strength of the associations between grade of EAR of the CC patients and each SNP or haplotype were assessed using the FE test and odds ratio (OR), respectively. Distribution of a test statistic was estimated by evaluating the statistics for a random sampling of 10,000 iterations. These statistical analyses were performed using SNPAlyze software, version 6.0 (DYNACOM, Chiba, Japan) (17). Pairwise LD analysis and haplotype/diplotype (a pair of haplotypes) analysis (expectation-maximization algorithm) were performed using SNPAlyze, haplo.stats (http://mayoresearch.mayo.edu/mayo/research/biostat/) (18), Haploview, version 4.2 (http://www.broadinstitute.org/haploview/haploview) (19), and UCSC Genome Browser Gateway (http://genome.ucsc.edu/cgi-bin/hgGateway).

A multiple logistic regression analysis was used to test for associations between diplotypes and EAR. Statistical analyses were carried out using the R software package (http://www.r-project.org/) and SAS version 9.2 (SAS Institute Inc, Cary, NC). A p value <0.05 was regarded as statistically significant.

RESULTS

Clinical factors and adverse reactions

A total of 243 CC patients who received pelvic RT were initially enrolled for this study. Of those, 35 patients were initially excluded from the analysis as follows: 26 patients who underwent hysterectomy before or after RT, 2 patients with double cancer, 3 patients who had prior/unusual RT, 2 patients treated with intra-arterial chemotherapy, and 2 patients with poor general condition at RT. The overall distribution of diarrhea in the remaining 208 patients was Grade 0 in 61 patients (29.3%), Grade 1 in 89 (42.8%), Grade 2 in 56 (26.9%), and Grade 3 in 2 patients (1.0%). None of the clinical factors indicated in Table E1 were identified as being associated with EAR ($p > 0.05$, FE, KW, MU, or CA test). The patients were divided into lower and higher AR groups for genetic analysis, after no significant differences in clinical features were found between the two groups (Table 1).

Allele and genotype frequencies

A total of 206 functional SNP candidates were selected from 32 genes that are applicable for our typing system (14, 16). These candidate SNPs were used to genotype the healthy donors and CC patients. Of these, 162 SNPs that were nonpolymorphic or showed less than 5% of the minor allele frequency in the CC patients were excluded from further analysis. The genotype distributions of the remaining 44 SNPs within 19 genes were in Hardy-Weinberg equilibrium in both the patient and control groups. Finally, 21 cSNPs were selected from the genes *AURKA, BRCA1, CDC25C, CDKN1A, CENPE, ESPL1, NPAT, OGG1, TP53, XRCC1, XRCC3*, and *ZNF830*, and 23 rSNPs were chosen from *ATM, AURKA, CD44, CDKN3, CENPE, GADD45A, MAD2L2, NPAT, OGG1, PTTG1*, and *TGFB1*. Table 2 details the SNP ID and the nucleotide and amino acid substitutions resulting from the polymorphisms.

Allele and genotype distributions for each SNP were compared between the lower and higher AR groups (Table 3). Among the 44 SNPs, seven SNPs were statistically significant for allelic associations; of those, rs189037 within *NPAT* and rs2273535 within *AURKA* fit a recessive model for genotype testing. When we performed multiple comparisons, these seven SNPs were not considered as definitive positives. Interestingly, however, they localize within two narrow chromosomal regions: five of the seven associated SNPs lie between the *NPAT-ATM* genes, which are 0.5 kb apart with opposite transcriptional directions on chromosome 11q22–23 (20–22), and the other two SNPs lie within exon 5 of the *AURKA* gene (NM_198433.1) on chromosome 20q13. It has been reported that haplotype analysis increases the statistical power (23–25) and that genetic analysis of haplotype frequencies enables the detection of predisposing haplotypes by using SNPs for which single-locus analysis shows no association (26). We therefore undertook a haplotype estimation analysis in these two chromosomal regions.

Table 1. Characteristics of lower and higher AR groups

Characteristic	Lower AR group* (n = 150)	Higher AR group* (n = 58)	Difference (p)
Age at RT (y): median (range)	60 (31–88)	60 (32–77)	0.35 (MU)
Smoking habit			0.70 (FE)
Yes	20 (13%)	10 (17%)	
Ever	17 (11%)	5 (9%)	
Never	109 (73%)	42 (72%)	
Unknown	4 (3%)	1 (2%)	
FIGO classification			0.29 (FE)
I, II	61 (41%)	16 (28%)	
III	62 (41%)	32 (55%)	
IVA	8 (5%)	3 (5%)	
IVB	18 (12%)	7 (12%)	
Unknown	1 (1%)	0 (0%)	
Treatment			0.76 (FE)
Radiotherapy†	82 (55%)	30 (52%)	
Chemoradiation therapy‡	68 (45%)	28 (48%)	
External beam (Gy) median (range)	50.6 (39.6–70.0)	50.6 (48.6–63.0)	0.84 (MU)
Brachytherapy (Gy) median (range)	24.0 (10.0–54.0)	24.0 (18.0–31.0)	0.84 (MU)

Abbreviations: FIGO = international federation of gynecology and obstetrics; AR = adverse reaction; RT = radiotherapy; MU = mann-Whitney U test; FE = fisher exact test.

* Lower AR group (Grade ≤1), higher AR group (Grade ≥2).

† Radiotherapy consisted of irradiation to the whole pelvis, plus an additional dose to parametria with central shielding, along with ^{192}Ir high-dose-rate intracavitary brachytherapy.

‡ Patients received radiotherapy (RT) as for the RT group, plus chemotherapy consisting of five administrations of cisplatin (40 mg/m^2) at 1-week intervals.

Table 2. Candidate genes and SNPs for the association study

Gene	Protein name*	rsSNP ID	Chr	RV	Amino acid or nucleotide substitution
MAD2L2	Mitotic spindle assembly checkpoint protein MAD2B	rs746218	1	CT	C-1853T
		rs2233004	1	AG	A-803G
		rs2233006	1	AT	A-525T
GADD45A	Growth arrest and DNA-damage-inducible, alpha	rs581000	1	GC	G-612C
CENPE	Centromere-associated protein E	rs2276974	4	CT	C-191T
		rs2615542	4	TC	Phe1535Leu
		rs1381657	4	GC	Ser1911Thr
		rs2243682	4	CT	Thr2090Met
CDC25C	M-phase inducer phosphatase 3	rs3734166	5	TC	Cys70Arg
PTTG1	Securin	rs3811999	5	CT	C-1993T
		rs2910199	5	GA	G-1785A
		rs1862392	5	TA	T-672A
		rs1862391	5	AC	A-398C
CDKN1A	Cyclin-dependent kinase inhibitor 1 (p21)	rs1801270	6	CA	Ser31Arg
NPAT	Protein NPAT	rs625120	11	CT	C-1855T
		rs189037	11	CT	C-468T
		rs4144901	11	AT	Leu540Phe
		rs2070661	11	AG	Ile575Val
ATM	Serine-protein kinase ATM	rs183460	11	CA	C-2849A
		rs228589	11	TA	T-351A
ESPL1	Separin (Separase)	rs1318648	12	AC	Arg614Ser
		rs17125266	12	GA	Met693Ile
CDKN3	Cyclin-dependent kinase inhibitor 3	rs2884513	14	GA	G-1323A
		rs2235961	14	AG	A-96G
TP53	Cellular tumor antigen p53 (Tumor suppressor p53)	rs1042522	17	GC	Arg72Pro
ZNF830	Zinc finger protein 830	rs931196	17	GT	Gln99His
	(Coiled-coil domain-containing protein 16)	rs3744355	17	GC	Ser154Thr
BRCA1	Breast cancer type 1 susceptibility protein	rs799917	17	CT	Pro871Leu
		rs16941	17	AG	Glu1038Gly
		rs16942	17	AG	Lys1183Arg
		rs1799966	17	AG	Ser1613Gly
AURKA	Aurora kinase A	rs2236208	20	AG	A-542G
	(Serine/threonine-protein kinase 6)	rs2236207	20	CT	C-214T
		rs2273535	20	AT	Ile31Phe
		rs1047972	20	GA	Val57Ile
OGG1	N-glycosylase/DNA lyase	rs159153	3	TC	T-1753C
		rs1052133	3	CG	Ser326Cys
CD44	CD44 antigen	rs1425802	11	TC	T-2016C
		rs60760313	11	GA	G-1967A
XRCC3	DNA repair protein XRCC3	rs861539	14	CT	Thr241Met
TGFB1	Transforming growth factor beta-1	rs1800469	19	CT	C-465T
XRCC1	DNA repair protein XRCC1	rs3810378	19	CG	C-1871G
		rs2682585	19	CT	C-1558T
		rs25487	19	GA	Arg399Gln

Abbreviations: rsSNP = reference single nucleotide polymorphisms; ID = identifier; Chr = chromosome; R = reference allele; V = variant allele.

* UniProtKB/Swiss-Prot database (www.Uniprot.org).

Association between haplotypes in NPAT-ATM and the risk of EAR

The LDs among the 17 SNPs in the *NPAT-ATM* region were measured by *D'* and r^2 using the allele frequency data from the CC patients, and LD maps were constructed (Fig. E1). The *D'* estimates of LD revealed a major haplotype block covering all of the SNPs in *NPAT-ATM* and thus spanning approximately 200 kb of chromosome 11. The HapMap constructed from the healthy donor data (27) also showed that the *NPAT* and *ATM* genes lie within a large single LD block in HAN Chinese/Japanese and Caucasian populations (Fig. E1 C and D). We analyzed 13 cSNPs in *NPAT* and 33 cSNPs in *ATM*, which together span almost all of the 200-kb region; however, 44 of these 46 cSNPs were not polymorphic in the CC patients or in our 133 Japanese healthy donors (data not shown). Indeed, only one of the two remaining cSNPs, rs2070661, showed a polymorphic association (Table 3).

Interestingly, the four other risk-associated SNPs on chromosome 11 are localized in the putative promoter region of the two genes with opposite transcriptional directions. We had initially estimated haplotypes comprising five SNPs including one cSNP, rs2070661 (Ile575Val), and four rSNPs (rs625120, rs189037, rs228589, and rs183460) localized in

Table 3. Association of SNPs between lower and higher AR groups

Gene(s)	rsSNP ID	Allele (R/V)				Genotype (RR/RV/VV)		Dominant model		Recessive model	
		Lower AR group	Higher AR group	OR (95% CI)	*p*	Lower AR group	Higher AR group	OR (95% CI)	*p*	OR (95% CI)	*p*
MAD2L2	rs746218	265/35	98/18	1.5 (0.73–2.6)	0.33	117/31/2	40/18/0	1.7 (0.77–3.1)	0.21	NC	1.0
	rs2233004	257/43	100/16	0.99 (0.47–1.7)	1.0	110/37/3	43/14/1	0.99 (0.53–2.2)	1.0	0.56 (0.19–2.4)	1.0
	rs2233006	164/136	71/45	0.74 (0.49–1.2)	0.27	47/70/33	24/23/11	0.68 (0.35–1.2)	0.19	0.87 (0.34–1.7)	0.71
GADD45A	rs581000	195/105	75/41	0.98 (0.63–1.6)	1.0	65/65/20	23/29/6	1.2 (0.62–2.3)	0.64	0.81 (0.21–1.8)	0.65
CENPE	rs2276974	232/68	92/24	0.84 (0.50–1.5)	0.70	87/58/5	38/16/4	0.8 (0.36–1.3)	0.35	2.9 (0.45–11)	0.27
	rs2615542	232/68	92/24	0.91 (0.51–1.5)	0.70	87/58/5	38/16/4	0.8 (0.37–1.4)	0.35	2.9 (0.42–11)	0.27
	rs1381657	273/27	105/11	1.1 (0.44–2.1)	0.85	125/23/2	48/9/1	1.1 (0.41–2.2)	1.0	2.4 (0.51–8.1)	1.0
	rs2243682	232/68	92/24	0.84 (0.50–1.5)	0.70	87/58/5	38/16/4	0.8 (0.36–1.3)	0.35	2.9 (0.42–11)	0.27
CDC25C	rs3734166	156/144	55/61	1.2 (0.79–1.9)	0.44	36/84/30	12/31/15	1.3 (0.60–2.8)	0.71	1.5 (0.64–2.8)	0.35
PTTG1	rs3811999	264/36	93/23	1.9 (0.98–3.2)	0.059	114/36/0	37/19/2	1.9 (0.92–3.5)	0.085	NC	0.077
	rs2910199	242/58	96/20	0.90 (0.47–1.5)	0.68	97/48/5	40/16/2	0.86 (0.42–1.6)	0.63	1.6 (0.31–5.5)	1.0
	rs1862392	242/58	96/20	0.90 (0.47–1.5)	0.68	97/48/5	40/16/2	0.86 (0.40–1.6)	0.63	1.6 (0.31–5.5)	1.0
	rs1862391	242/58	96/20	0.90 (0.47–1.5)	0.68	97/48/5	40/16/2	0.86 (0.40–1.5)	0.63	1.6 (0.31–5.5)	1.0
CDKN1A	rs1801270	171/129	59/57	1.3 (0.82–2.0)	0.27	51/69/30	16/27/15	1.5 (0.71–2.8)	0.41	1.5 (0.64–2.9)	0.35
NPAT	rs625120	141/159	69/47	**0.59 (0.39–0.94)**	**0.029**	35/71/44	21/27/10	0.57 (0.27–1.1)	0.081	0.53 (0.20–1.0)	0.080
	rs189037	179/121	55/61	**1.7 (1.1–2.5)**	**0.028**	55/69/26	15/25/18	1.8 (0.88–3.5)	0.19	**2.3 (1.04–4.4)**	**0.038**
	rs4144901	239/61	101/15	0.60 (0.29–1.0)	0.090	95/49/6	45/11/2	0.52 (0.22–0.96)	0.069	0.80 (0.25–4.1)	1.0
	rs2070661	147/153	70/46	**0.61 (0.40–0.97)**	**0.049**	39/69/42	22/26/10	0.61 (0.30–1.1)	0.13	0.56 (0.22–1.1)	0.15
ATM	rs183460	145/155	69/47	**0.62 (0.41–0.98)**	**0.049**	38/69/43	21/27/10	0.63 (0.31–1.2)	0.13	0.54 (0.21–1.0)	0.11
	rs228589	146/154	69/47	**0.63 (0.42–0.99)**	**0.050**	39/68/43	21/27/10	0.66 (0.33–1.2)	0.17	0.54 (0.21–1.1)	0.11
ESPL1	rs1318648	239/61	101/15	0.60 (0.29–1.0)	0.090	95/49/6	43/15/0	0.63 (0.28–1.1)	0.19	NC	0.19
	rs17125266	241/59	102/14	0.51 (0.27–1.0)	0.084	96/49/5	44/14/0	0.59 (0.26–1.1)	0.14	NC	0.33
CDKN3	rs2884513	219/81	85/31	0.99 (0.64–1.7)	1.0	82/55/13	33/19/6	0.96 (0.49–1.7)	0.88	1.4 (0.32–3.3)	0.79
	rs2235961	210/90	79/37	1.1 (0.68–1.7)	0.72	79/52/19	28/23/7	1.3 (0.65–2.2)	0.64	0.98 (0.44–3.3)	1.0
TP53	rs1042522	179/121	81/35	0.62 (0.40–1.0)	0.056	50/79/21	26/29/3	0.64 (0.33–1.1)	0.15	0.38 (0.09–0.95)	0.091
ZNF830	rs931196	277/23	112/4	0.46 (0.10–1.1)	0.18	127/23/0	55/2/1	0.34 (0.08–0.84)	0.060	NC	0.28
	rs3744355	216/84	85/31	0.96 (0.56–1.5)	0.90	75/66/9	31/23/4	0.91 (0.46–1.6)	0.76	1.4 (0.25–4.0)	0.76
BRCA1	rs799917	207/93	77/39	1.1 (0.71–1.8)	0.64	67/73/10	26/25/7	0.96 (0.54–1.9)	1.0	2.2 (0.58–5.6)	0.26
	rs16941	207/93	77/39	1.1 (0.70–1.8)	0.64	67/73/10	26/25/7	0.96 (0.54–1.9)	1.0	2.2 (0.58–5.6)	0.26
	rs16942	207/93	77/39	1.1 (0.71–1.8)	0.64	67/73/10	26/25/7	0.95 (0.53–1.9)	1.0	2.2 (0.57–5.3)	0.26
	rs1799966	207/93	77/39	1.1 (0.70–1.8)	0.64	67/73/10	26/25/7	0.96 (0.54–1.9)	1.0	2.2 (0.57–5.6)	0.26
AURKA	rs2236208	272/28	111/5	0.46 (0.10–1.0)	0.11	125/22/3	53/5/0	0.50 (0.11–1.2)	0.19	NC	0.56
	rs2236207	272/28	111/5	0.46 (0.10–1.0)	0.11	125/22/3	53/5/0	0.50 (0.11–1.2)	0.19	NC	0.56
	rs2273535	177/123	83/33	**0.55 (0.35–0.90)**	**0.018**	56/65/29	27/29/2	0.72 (0.37–1.3)	0.27	**0.18 (0.06–0.46)**	**0.0039**
	rs1047972	250/50	107/9	**0.43 (0.16–0.82)**	**0.019**	108/34/8	49/9/0	0.50 (0.17–0.98)	0.073	NC	0.11
OGG1	rs159153	274/26	105/11	1.2 (0.46–2.2)	0.85	125/24/1	47/11/0	1.2 (0.48–2.5)	0.69	NC	1.0
	rs1052133	159/141	69/47	0.8 (0.49–1.2)	0.27	44/71/35	19/31/8	0.92 (0.45–1.7)	0.62	0.55 (0.18–1.1)	0.18
CD44	rs1425802	174/126	63/53	1.1 (0.74–1.8)	0.51	50/74/26	22/19/17	0.87 (0.43–1.6)	0.63	2.1 (0.95–4.0)	0.084
	rs60760313	272/28	102/14	1.4 (0.61–2.6)	0.47	125/22/3	44/14/0	1.7 (0.73–3.3)	0.24	NC	0.56
XRCC3	rs861539	264/36	108/8	0.57 (0.19–1.1)	0.16	116/32/2	50/8/0	0.57 (0.18–1.2)	0.18	NC	1.0

(*Continued*)

Table 3. Association of SNPs between lower and higher AR groups (*Continued*)

Gene(s)	rsSNP ID	Allele (R/V)				Genotype (RR/RV/VV)		Dominant model		Recessive model	
		Lower AR group	Higher AR group	OR (95% CI)	*p*	Lower AR group	Higher AR group	OR (95% CI)	*p*	OR (95% CI)	*p*
TGFB1	rs1800469	151/149	57/59	1.1 (0.68–1.6)	0.91	35/81/34	15/27/16	0.95 (0.44–1.9)	0.72	1.4 (0.62–3.7)	0.47
XRCC1	rs3810378	218/82	81/35	1.2 (0.71–1.8)	0.63	80/58/12	29/23/6	1.2 (0.62–2.1)	0.76	1.5 (0.38–3.7)	0.59
	rs2682585	272/28	104/12	1.2 (0.49–2.2)	0.72	122/28/0	46/12/0	1.2 (0.49–2.4)	0.84	NC	NC
	rs25487	221/79	84/32	1.1 (0.64–1.7)	0.81	83/55/12	31/22/5	1.1 (0.59–2.0)	0.88	1.2 (0.25–3.3)	1.0

Abbreviations: rsSNP = reference single nucleotide polymorphisms; ID = identifier; R = reference allele; V = variant; RR = homozygous of R, RV = heterozygous; VV = homozygous of V; OR = odds ratio; CI = confidence interval; NC = insufficient sample size to perform calculation; AR = adverse reaction.
Statistical significance and the strength of the associations were assessed using Fisher exact test. The OR and 95% CI of the OR was calculated by bootstrap method (10,000).

this same region. However, because adding rs2070661 (Ile575Val) to the haplotype construction did not affect the frequencies of the estimated haplotypes in both AR groups, further haplotype analyses focused only on the remaining four rSNPs.

Haplotypes showing a possible risk of AR and the effect of each haplotype are presented in Table 4. The estimated four major haplotypes cover 99.3% of the chromosomes in the CC group, and the association analysis implicated haplotype 2 (H2) in the *NPAT-ATM* region in significantly increasing the risk of EAR compared with the other haplotypes (OR = 1.86; 95% CI, 1.21–2.87).

The estimated diplotype frequencies of H2 were also compared between the lower and higher AR groups (Table 5). The risk of EAR was significantly higher in CC patients with two H2 types than in those with no or one H2 type (OR = 2.81; 95% CI, 1.26–5.50).

Association between haplotypes in AURKA and the risk of EAR

Figure E2 shows a graphic representation of LDs in *AURKA* using both D' and r^2. A lower LD was observed with the combination of rs2273535 (Ile31Phe) and rs1047972 (Val57Ile) in our CC patients, Han Chinese/Japanese, and Caucasian populations (the HapMap data).

Haplotype analysis using the haplo.stat program revealed three haplotypes covering almost 100% of the chromosomes in the CC group (Table 4). Haplotype 1 (H1) in *AURKA* significantly increased the risk of EAR compared with the other haplotypes (OR = 1.75; 95% CI, 1.10–2.78), and haplotype 3 (H3) significantly decreased the risk of EAR (OR = 0.42; 95% CI, 0.20–0.89). Therefore, CC patients with H1 have a significantly greater risk of EAR than do those with H3 (OR = 2.60; 95% CI, 1.19–6.30).

Estimated diplotype frequencies for H1 and H3 were compared between the lower and higher AR groups (Table 5). The risk of EAR was significantly greater in the patients with one or two H1 types than in those with no H1 type (OR = 5.57; 95% CI, 2.17–17.99). Diplotypes of H3 showed no statistically significant association with risk of EAR in CC patients; presumably the H3 type carried a low frequency.

Combined effects of the diplotypes of NPAT–ATM and AURKA on the risk of EAR

The possibility of combined effects of the diplotypes of *NPAT–ATM* and *AURKA* were tested by multiple logistic regression analysis. Individuals with both risk diplotypes had a significantly increased risk of EAR than did those individuals with other diplotypes (OR = 3.24; 95% CI, 1.52–6.92; Table 6).

DISCUSSION

To our knowledge, this study is the first demonstration of genetic association between variants in *NPAT-ATM* and *AURKA* and risk of an early adverse intestinal reaction in

Table 4. Estimated haplotypes and frequency of haplotypes and association with risk of early adverse reaction

Gene	Haplotype	SNP				Estimated frequency (%)*				
						Pool	Lower AR group	Higher AR group	OR (95% CI)	Permutation *p*-value (10,000)
		rs625120	rs189037	rs228589	rs183460					
NPAT-ATM	H1	T	C	T	T	48.1	51.0	40.5	0.65 (0.42–1.01)	0.064
	H2	C	T	A	G	41.6	37.3	52.6	**1.86 (1.21–2.87)**	**0.005**
	H3	C	C	A	G	8.2	8.7	6.9	0.78 (0.34–1.78)	0.686
	H4	T	T	A	G	1.4	2.0	0.0	NC	0.192
		rs2273535	rs1047972							
AURKA	H1	A	G			62.5	59.0	71.6	**1.75 (1.10–2.78)**	**0.020**
	H2	T	G			23.3	24.3	20.7	0.81 (0.48–1.37)	0.517
	H3	T	A			14.2	16.7	7.8	**0.42 (0.20–0.89)**	**0.020**

Abbreviations: OR = odds ratio; CI = confidence interval; NC = insufficient sample size to perform calculation; AR = adverse reaction.
* Haplotypes observed with >1% frequency in pool.

CC patients who have undergone RT. Detection of multiple SNPs in two chromosomal loci associated with increased risk allowed us to estimate haplotype and related diplotype frequencies in the lower and higher AR groups. Each risk diplotype of the *NPAT-ATM* and *AURKA* genes independently contributed to that risk.

Meanwhile, 7 of 24 patients in the lower AR group with neither risk diplotype of *NPAT-ATM* and *AURKA* carried instead the reduced risk type of *AURKA* (H3/H3 diplotype), whereas no patients in the higher AR group had the H3/H3 diplotype of *AURKA*. Taken together, these data suggested that CC patients could be stratified with respect to risk of EAR after RT by different *NPAT-ATM* and *AURKA* genotype combinations.

In this study, we hypothesized that variations in the genes related to cell cycle regulation or genome maintenance could contribute to heterogeneity in the risk of adverse intestinal reactions to RT, and we identified risk-associated SNPs in *NPAT-ATM* and *AURKA*. However, we found no significant association between the SNPs in *MAD2L2, PTTG1*, *RAD9A*, or *LIG3* (14) and the risk of EAR. Moreover, SNPs in *CD44* that were also identified in our previous study (14) and classified into the inflammatory response category were not associated with a risk of an adverse intestinal reaction (Table 3). Collectively, these data could indicate that variations in genes associated with the risk of radiation injuries are expressed phenotypically in a tissue-specific manner.

NPAT has been functionally implicated in progression through the G1 and S phases of the cell cycle and for S phase entry (28, 29). In this study, a haplotype comprising four SNPs upstream of and in the first intron of *NPAT,* rs625120 (C-1855T), rs189037 (C-468T), rs228589 (in the first intron of *NPAT*), and rs183460 (in the first intron of *NPAT*) was significantly associated with an increased risk of AR. *In silico* analysis indicated that the transcriptional regulator of the adaptive response to hypoxia, hypoxia-inducible factor 1 beta (HIF-1 beta), could bind to a six-base sequence containing the T-468 allele (rs189037) but not to the C-468 allele-containing sequence (30). HIF-1 is known to activate the transcription of genes involved in such functions as cell survival, cell proliferation, drug resistance, nucleotide metabolism, and glucose metabolism under hypoxic conditions (31). It is therefore possible that

Table 5. Estimated frequency of diplotypes and association with risk of early adverse reaction

Gene	Diplotype	Estimated frequency (%)			Dominant model		Recessive model	
		Pool	Lower AR group	Higher AR group	OR (95%CI)	*p*	OR (95%CI)	*p*
NPAT-ATM	-/-	36.1	40.0	25.9				
	H2/-	44.7	45.3	43.1	2.08 (1.00–4.05)	0.076	**2.81 (1.26–5.50)**	**0.010**
	H2/H2	19.2	14.7	31.0				
AURKA	-/-	14.9	19.3	3.4				
	H1/-	45.2	43.3	50.0	**5.57 (2.17–17.99)**	**0.004**	1.39 (0.78–2.75)	0.269
	H1/H1	39.9	37.3	46.6				
	-/-	75.5	72.0	84.5				
	H3/-	20.7	22.7	15.5	0.50 (0.18–0.97)	0.073	NC	0.109
	H3/H3	3.8	5.3	0.0				

Abbreviations: OR = odds ratio; CI = confidence interval; NC = insufficient sample size to perform calculation; AR = adverse reaction.
Statistical significance and the strength of the associations were assessed using the Fisher exact test. The OR and 95% CI of the OR was calculated by the bootstrap method (10,000).